Alterations in schizophrenia-associated genes can lead to increased power in delta oscillations. Supplementary material

S1 Supplementary methods

S1.1 The single cell model

S1.1.1 The ion channels included in the L5PC model and their genetic etiology

The neuron model (Hay et al., 2011) that we employ is a multicompartmental Hodgkin-Huxley type of model with a reconstructed layer V thick-tufted pyramidal neuron morphology. It includes the following ionic currents: Fast inactivating Na^+ current (I_{Nat}), persistent Na^+ current (I_{Nap}), non-specific cation current (I_{h}), muscarinic K^+ current (I_{m}), slow inactivating K^+ current (I_{Kp}), fast inactivating K^+ current (I_{Kt}), fast non-inactivating K^+ current ($I_{\mathrm{Kv3.1}}$), high-voltage-activated Ca^{2+} current (I_{CaHVA}), low-voltage-activated Ca^{2+} current (I_{CaLVA}), small-conductance Ca^{2+}-activated K^+ current (I_{SK}), and the passive leak current (I_{leak}).

To date, there is no clear consensus on which particular ion channel subunits underlie each of these currents in L5PCs, but strong indications can be obtained from experiments where the expression of different ion channel subunits in L5PCs were studied. mRNAs of ion channel-encoding genes *KCNA2*, *KCND2*, *KCND3*, *CACNA1A*, *CACNA1B*, *CACNA1C*, *CACNA1D*, *CACNA1E*, *CACNA1G*, *CACNA1H*, *CACNA1I*, *HCN1*, and *HCN2* were observed in L5PCs in a study of postnatal rat neocortices at different stages of development (Christophe et al., 2005). Of these, *CACNA1A*, *CACNA1B*, *CACNA1C*, and *CACNA1D* are known to contribute to I_{CaHVA}, and *CACNA1G*, *CACNA1H*, and *CACNA1I* contribute to I_{CaLVA}, while the genes *KCNA2*, *KCND2*, and *KCND3* might contribute to the slow I_{Kp} current. Note that the molecular basis of LVA Ca^{2+} currents in L5PCs is still disputed. In a recent experiment, T-type Ca^{2+} currents were not detected either in the soma or its neighbourhood (Almog, Korngreen, et al., 2009). In Hay et al., 2011, however, the LVA channel kinetics were based on measurements carried out on T-type Ca^{2+} channels. In this work, based on the expression data of *CACNA1I* in L5PCs (Christophe et al., 2005), we consider the I_{CaLVA} current as a target of the T-type Ca^{2+} channel gene *CACNA1I*.

Expression of *KCNC1* was confirmed in certain subpopulations of L5PCs (Akemann et al., 2004), and expression of *KCNB1* and *KCNB2* has been observed in layer V or VI pyramidal neurons (Guan et al., 2007). The slow activation kinetics of channels composed of *KCNB1* and *KCNB2* subunits makes them likely contributors to the I_{Kp} current, while *KCNC1*-based channels form the $I_{\mathrm{Kv3.1}}$ current included in the Hay model. Expression of muscarinic potassium channel-encoding genes *KCNQ2* and *KCNQ3* was observed in L5PCs in Battefeld et al., 2014, and these genes are known to contribute to the I_{m} current.

Expression of sodium channel subunit-encoding genes *SCN2A* and *SCN8A* was observed in pyramidal cells of all layers of human epileptic tissue (Tian et al., 2014). In another study, the genes *SCN1A*, *SCN2A*, *SCN3A*, and *SCN6A* were found to be expressed in L5PCs (Whitaker et al., 2000), while expression of *SCN1A* was not observed in Tian et al., 2014. Of the genes encoding sodium α subunits, *SCN1A*, *SCN2A* and *SCN3A*, alongside with *SCN9A*, are tetrodotoxin-sensitive (Catterall et al., 2005) and hence form both the transient (I_{Nat}) and persistent (I_{Nap}) Na^+ currents. Whether these genes contribute to I_{Nat} or I_{Nap} may depend on the modulatory subunits that they are associated with (Ma et al., 1997). Expression of *KCNN1* and *KCNN2* has been observed in L5PCs, while the expression of the third gene affecting the I_{SK} current, *KCNN3*, is weak throughout the neocortex but more prominent in pyramidal neurons in CA1 (Ballesteros-Merino et al., 2014).

Most of the above genes code for the α subunit of the underlying ion channel. Many ion channels also incorporate modulatory subunits, the presence of which may change the kinetics or voltage-dependence of the ion channel. As an example, the $\beta 2$ subunit of Ca^{2+} channels, encoded by *CACNB2*, associates with L-type Ca^{2+} channels (where the α pore is encoded by *CACNA1S*, *CACNA1C*, *CACNA1D* or *CACNA1F*). In a similar fashion, the $\alpha_2\delta$ subunits of Ca^{2+} channels, encoded by genes *CACNA2D*1–4, modulate the number and function of the high-voltage activated Ca^{2+} channels inserted into the membrane (Geisler et al., 2015).

In addition to describing the dynamics of these ionic channels, the model (Hay et al., 2011) also describes the dynamics of the intracellular Ca^{2+} concentration, $[Ca^{2+}]_i$. According to the model, $[Ca^{2+}]_i$ is increased by the current flow through Ca^{2+} channels, and is otherwise decreased towards a resting-state level of $[Ca^{2+}]_i$. This extrusion of Ca^{2+} is contributed by many proteins and intracellular signalling molecules, but two types of proteins possess a key role, namely, sarco/endoplasmic reticulum Ca^{2+} ATPase (SERCA) and plasma membrane Ca^{2+} ATPase (PMCA). The SERCA proteins pump cytosolic Ca^{2+} into the sarcoplasmic or endoplasmic reticulum, which later may release the excessive Ca^{2+} to strengthen the Ca^{2+} pulses entering through the voltage-gated Ca^{2+} channels. SERCA pumps are encoded by genes ATP2A1, ATP2A2, and ATP2A3, of which ATP2A2 is widely expressed in the brain (Baba-Aissa et al., 1998). PMCA proteins pump intracellular Ca^{2+} into the extracellular medium, and are encoded by genes ATP2B1, ATP2B2, ATP2B3, and ATP2B4, all of which are widely expressed in the brain (Stahl et al., 1992; Stahl et al., 1994).

S1.1.2 The model formulation

The current balance equation for each compartment of the model neuron can be written as

$$C_m \frac{\partial V}{\partial t} = I_{\mathrm{Nat}} + I_{\mathrm{Nap}} + I_h + I_m + I_{\mathrm{Kp}} + I_{\mathrm{Kt}} + I_{\mathrm{Kv3.1}} + I_{\mathrm{CaHVA}} + I_{\mathrm{CaLVA}} + I_{\mathrm{SK}} + I_l + I_{axial},$$

where each type of current, except for the axial current, can be described as a multiplication of activation and inactivation variables as

$$I = \bar{g} m^{N_m} h^{N_h} (E - V).$$

Here, $\bar{g}$ is the maximal conductance of the ion channels, m and h are the activation and inactivation variables while N_m and N_h are constants describing their sensitivities, and E is the reversal potential corresponding to the ionic species. Reversal potentials of Na^+ and K^+ are constants ($E_{Na} = 50$ mV, $E_K = -85$ mV), while the reversal potential of Ca^{2+} depends on the intracellular $[Ca^{2+}]$: E_{Ca} varied between 96 mV and 120 mV in our single-cell simulations. The dynamics of the activation and inactivation variables are defined as

$$\frac{dm}{dt} = \frac{m - m_\infty}{\tau_m} \qquad \text{and} \qquad \frac{dh}{dt} = \frac{h - h_\infty}{\tau_h},$$

where m_∞, h_∞, τ_m, and τ_h are functions of the membrane potential V. Typically, functions m_∞ and h_∞ have a sigmoidal shape, where the half-activation and half-inactivation voltages are determined by one or more (depending on ion channel) parameters each. We denote these parameters $V_{\mathrm{offm}*}$ and $V_{\mathrm{offh}*}$, where $*$ stands for further specifications if there are multiple parameters affecting the half-(in)activation voltage. In a similar fashion, parameters $V_{\mathrm{slom}*}$ and $V_{\mathrm{sloh}*}$ affect the slopes of the (in)activation curves, and parameters $\tau_{\mathrm{m}*}$ and $\tau_{\mathrm{offh}*}$ influence the time constants. As an exception, the activation of I_{SK} is solely dependent on the intracellular $[Ca^{2+}]$, and this dependence is quantified by the half-activation concentration parameter c_{off} and the slope parameter c_{slo}. The intracellular $[Ca^{2+}]$ obeys the following dynamics:

$$\frac{d[Ca^{2+}]_i}{dt} = \frac{I_{\mathrm{CaHVA}} + I_{\mathrm{CaLVA}}}{2\gamma F d} - \frac{[Ca^{2+}]_i - c_{\mathrm{min}}}{\tau_{\mathrm{decay}}}, \tag{S1}$$

where I_{CaHVA} and I_{CaLVA} are the high and low-voltage activated Ca^{2+} currents entering the considered cell segment, γ represents the fraction of Ca^{2+} ions entering the cell that contribute to the intracellular $[Ca^{2+}]$, F the Faraday constant, d is the depth of the sub-membrane layer considered for calculation of concentration, c_{min} the resting intracellular $[Ca^{2+}]$, and τ_{decay} is the decay time constant of the intracellular $[Ca^{2+}]$. The simulation codes are provided in the ModelDB entry 237469 (https://senselab.med.yale.edu/ModelDB/showModel.cshtml?model=237469).

S1.1.3 Channel activation and inactivation dynamics

Instead of the reconstructed morphology as presented in Hay et al., 2011, we use the reduced morphology and the maximal conductances of the ion channels as presented and fitted in Mäki-Marttunen et al., 2018. This reduced model consists of four compartments, namely, the soma, apical trunk, apical tuft, and basal dendrite, each consisting of $nseg = 5$ identical subcompartments. Here, the model equations and parameter values are listed for all ion channels. The maximal conductances $\bar{g}$ are different for different parts of the neuron: The subindex s refers to soma, a_0 to apical trunk, a_1 to apical tuft, and b to basal dendrite, and for each current type all unshown maximal conductances are zero.

Fast inactivating Na^+ current, I_{Nat}

$$\alpha_m = -\frac{1}{\tau_{\mathrm{ma}}} \cdot \frac{V_{\mathrm{offm}} - V}{1 - \exp(\frac{(V_{\mathrm{offm}} - V)}{V_{\mathrm{slom}}})}$$

$$\beta_m = \frac{1}{\tau_{\mathrm{mb}}} \cdot \frac{V_{\mathrm{offm}} - V}{1 - \exp(\frac{-(V_{\mathrm{offm}} - V)}{V_{\mathrm{slom}}})}$$

$$\alpha_h = \frac{1}{\tau_{\mathrm{ha}}} \cdot \frac{V_{\mathrm{offh}} - V}{1 - \exp(\frac{(V_{\mathrm{offh}} - V)}{V_{\mathrm{sloh}}})}$$

$$\beta_h = -\frac{1}{\tau_{\mathrm{hb}}} \cdot \frac{V_{\mathrm{offh}} - V}{1 - \exp(\frac{-(V_{\mathrm{offh}} - V)}{V_{\mathrm{sloh}}})}$$

$$m_\infty = \frac{\alpha_m}{\alpha_m + \beta_m}$$

$$h_\infty = \frac{\alpha_h}{\alpha_h + \beta_h}$$

$$\tau_m = \frac{1}{T_{\mathrm{adj}}(\alpha_m + \beta_m)}$$

$$\tau_h = \frac{1}{T_{\mathrm{adj}}(\alpha_h + \beta_h)}$$

$V_{\text{offm}} = -38$ mV, $V_{\text{offh}} = -66$ mV, $V_{\text{slom}} = 6.0$ mV, $V_{\text{sloh}} = 6.0$ mV, $\tau_{\text{ma}} = 5.49$ ms, $\tau_{\text{mb}} = 8.06$ ms, $\tau_{\text{ha}} = 66.67$ ms, $\tau_{\text{hb}} = 66.67$ ms, $\bar{g}_s = 2.41$ S/cm^2, $\bar{g}_{a_0} = 0.0135$ S/cm^2, $\bar{g}_{a_1} = 0.0131$ S/cm^2, $N_m = 3$, $N_h = 1$

Persistent Na^+ current, I_{Nap}

$$m_\infty = \frac{1}{1+\exp(\frac{V_{\text{offm}}-V}{V_{\text{slom}}})}$$

$$h_\infty = \frac{1}{1+\exp(-\frac{V_{\text{offh}}-V}{V_{\text{sloh}}})}$$

$$\alpha_m = -\frac{1}{\tau_{\text{ma}}} \cdot \frac{V_{\text{offma}} - V}{1-\exp(\frac{(V_{\text{offma}}-V)}{V_{\text{sloma}}})}$$

$$\beta_m = \frac{1}{\tau_{\text{mb}}} \cdot \frac{V_{\text{offmb}} - V}{1-\exp(\frac{-(V_{\text{offmb}}-V)}{V_{\text{slomb}}})}$$

$$\alpha_h = \frac{1}{\tau_{\text{ha}}} \cdot \frac{V_{\text{offha}} - V}{1-\exp(-\frac{V_{\text{offha}}-V}{V_{\text{sloha}}})}$$

$$\beta_h = -\frac{1}{\tau_{\text{hb}}} \cdot \frac{V_{\text{offhb}} - V}{1-\exp(\frac{V_{\text{offhb}}-V}{V_{\text{slohb}}})}$$

$$\tau_m = \frac{6}{T_{\text{adj}}(\alpha_m + \beta_m)}$$

$$\tau_h = \frac{1}{T_{\text{adj}}(\alpha_h + \beta_h)}$$

$V_{\text{offm}} = -52.6$ mV, $V_{\text{slom}} = 4.6$ mV, $V_{\text{offma}} = -38$ mV, $V_{\text{offmb}} = -38$ mV, $V_{\text{sloma}} = 6.0$ mV, $V_{\text{slomb}} = 6.0$ mV, $\tau_{\text{ma}} = 5.49$ ms, $\tau_{\text{mb}} = 8.06$ ms, $V_{\text{offh}} = -48.8$ mV, $V_{\text{sloh}} = 10.0$ mV, $V_{\text{offha}} = -17$ mV, $V_{\text{offhb}} = -64.4$ mV, $V_{\text{sloha}} = 4.63$ mV, $V_{\text{slohb}} = 2.63$ mV, $\tau_{\text{ha}} = 347222.2$ ms, $\tau_{\text{hb}} = 144092.2$ ms, $\bar{g}_s = 0.00206$ S/cm^2, $N_m = 3$, $N_h = 1$

Non-specific cation current, I_{h}

$$\alpha_h = -\frac{1}{\tau_{\text{ha}}} \cdot \frac{V_{\text{offha}} - V}{\exp(-\frac{V_{\text{offha}}-V}{V_{\text{sloha}}}) - 1}$$

$$\beta_h = \frac{1}{\tau_{\text{hb}}} \exp(-\frac{V_{\text{offhb}} - V}{V_{\text{slohb}}})$$

$$h_\infty = \frac{\alpha_h}{\alpha_h + \beta_h}$$

$$\tau_h = \frac{1}{\alpha_h + \beta_h}$$

$E = -45.0$ mV, $V_{\text{offha}} = -154.9$ mV, $V_{\text{sloha}} = 11.9$ mV, $\tau_{\text{ha}} = 155.52$ ms, $V_{\text{offhb}} = 0.0$ mV, $V_{\text{slohb}} = 33.1$ mV, $\tau_{\text{hb}} = 5.18$ ms, $\bar{g}_s = 0.000279$ S/cm^2, $\bar{g}_{a_1} = 0.00493$ S/cm^2, $\bar{g}_b = 0.000294$ S/cm^2, $N_m = 0$, $N_1 = 0$

Muscarinic K^+ current, I_{m}

$$\alpha_m = \frac{1}{\tau_{\text{ma}}} \exp(-\frac{V_{\text{offma}} - V}{V_{\text{sloma}}})$$

$$\beta_m = \frac{1}{\tau_{\text{mb}}} \exp(\frac{V_{\text{offmb}} - V}{V_{\text{slomb}}})$$

$$m_\infty = \frac{\alpha_m}{\alpha_m + \beta_m}$$

$$\tau_m = \frac{1}{T_{\text{adj}}(\alpha_m + \beta_m)}$$

$V_{\text{offma}} = -35$ mV, $V_{\text{sloma}} = 10$ mV, $\tau_{\text{ma}} = 303.03$ ms, $V_{\text{offmb}} = -35$ mV, $V_{\text{slomb}} = 10$ mV, $\tau_{\text{mb}} = 303.03$ ms, $\bar{g}_{a_0} = 0.000143$ S/cm^2, $\bar{g}_{a_1} = 0.000113$ S/cm^2, $N_m = 1$, $N_h = 0$

Slow inactivating K^+ current, I_{Kp}

$$m_\infty = \frac{1}{1+\exp(\frac{V_{\text{offm}}-V}{V_{\text{slom}}})}$$

$$h_\infty = \frac{1}{1+\exp(-\frac{V_{\text{offh}}-V}{V_{\text{sloh}}})}$$

$$\tau_m = \begin{cases} \frac{\tau_{\text{mmin}} + \tau_{\text{mdiff1}} \exp(-\frac{V_{\text{offmt}} - V}{V_{\text{slomt}}})}{T_{\text{adj}}}, & \text{if } V \leq V_{thresh} \\ \frac{\tau_{\text{mmin}} + \tau_{\text{mdiff2}} \exp(\frac{V_{\text{offmt}} - V}{V_{\text{slomt}}})}{T_{\text{adj}}}, & \text{if } V > V_{thresh} \end{cases}$$

$$\tau_h = \frac{\tau_{\text{hmin}} + (\tau_{\text{hdiff1}} - \tau_{\text{hdiff2}}(V_{\text{offht1}} - V)) \exp\left(-\left(\frac{V_{\text{offht2}} - V}{V_{\text{sloht}}}\right)^2\right)}{T_{\text{adj}}}$$

$$V_{thresh} = V_{\text{offmt}} - \frac{V_{\text{slomt}}}{2} \log\left(\frac{\tau_{\text{mdiff1}}}{\tau_{\text{mdiff2}}}\right)$$

$V_{\text{offm}} = -11$ mV, $V_{\text{slom}} = 12$ mV, $V_{\text{offmt}} = -10$ mV, $V_{\text{slomt}} = 38.46$ mV, $\tau_{\text{mmin}} = 1.25$ ms, $\tau_{\text{mdiff1}} = 175.03$ ms, $\tau_{\text{mdiff2}} = 13$ ms, $V_{\text{offh}} = -64$ mV, $V_{\text{sloh}} = 11$ mV, $V_{\text{offht1}} = -65$ mV, $V_{\text{offht2}} = -85$ mV, $V_{\text{sloht}} = 48$ mV, $\tau_{\text{hmin}} = 360$ ms, $\tau_{\text{hdiff1}} = 1010$ ms, $\tau_{\text{hdiff2}} = 24$ ms/mV, $\bar{g}_s = 0.000176$ S/cm^2, $N_m = 2$, $N_h = 1$

Fast inactivating $\mathbf{K}^+$ current, I_{Kt}

$$m_\infty = \frac{1}{1 + \exp(\frac{V_{\text{offm}} - V}{V_{\text{slom}}})}$$

$$h_\infty = \frac{1}{1 + \exp(-\frac{V_{\text{offh}} - V}{V_{\text{sloh}}})}$$

$$\tau_m = \frac{\tau_{\text{mmin}} + \tau_{\text{mdiff}} \exp\left(-\left(\frac{V_{\text{offmt}} - V}{V_{\text{slomt}}}\right)^2\right)}{T_{\text{adj}}}$$

$$\tau_h = \frac{\tau_{\text{hmin}} + \tau_{\text{hdiff}} \exp\left(-\left(\frac{V_{\text{offht}} - V}{V_{\text{sloht}}}\right)^2\right)}{T_{\text{adj}}}$$

$V_{\text{offm}} = -10$ mV, $V_{\text{slom}} = 19$ mV, $V_{\text{offh}} = -76$ mV, $V_{\text{sloh}} = 10$ mV, $V_{\text{offmt}} = -81$ mV, $V_{\text{slomt}} = 59$ mV, $\tau_{\text{mmin}} = 0.34$ ms, $\tau_{\text{mdiff}} = 0.92$ ms, $V_{\text{offht}} = -83$ mV, $V_{\text{sloht}} = 23$ mV, $\tau_{\text{hmin}} = 8$ ms, $\tau_{\text{hdiff}} = 49$ ms, $\bar{g}_s = 0.0239$ S/cm^2, $N_m = 4$, $N_h = 1$

Fast, non inactivating $\mathbf{K}^+$ current, $I_{\text{Kv3.1}}$

$$m_\infty = \frac{1}{1 + \exp(\frac{V_{\text{offm}} - V}{V_{\text{slom}}})}$$

$$h_\infty = \frac{1}{T_{\text{adj}}\left(1 + \exp(\frac{V_{\text{offh}} - V}{V_{\text{sloh}}})\right)}$$

$V_{\text{offma}} = 18.7$ mV, $V_{\text{offmt}} = -46.56$ mV, $V_{\text{sloma}} = 9.7$ mV, $V_{\text{slomt}} = 44.14$ mV, $\tau_{\text{mmax}} = 4.0$ ms, $\bar{g}_s = 0.701$ S/cm^2, $\bar{g}_{a_0} = 0.00121$ S/cm^2, $N_m = 1$, $N_h = 0$

High-voltage-activated $\mathbf{Ca}^{2+}$ current, I_{CaHVA}

$$\alpha_m = -\frac{1}{\tau_{\text{ma}}} \cdot \frac{V_{\text{offma}} - V}{1 - \exp(\frac{V_{\text{offma}} - V}{V_{\text{sloma}}})}$$

$$\beta_m = \frac{1}{\tau_{\text{mb}}} \exp(-\frac{V_{\text{offmb}} - V}{V_{\text{slomb}}})$$

$$m_\infty = \frac{\alpha_m}{\alpha_m + \beta_m}$$

$$\tau_m = \frac{1}{\alpha_m + \beta_m}$$

$$\alpha_h = \frac{1}{\tau_{\text{ha}}} \exp(\frac{V_{\text{offha}} - V}{V_{\text{sloha}}})$$

$$\beta_h = -\frac{1}{\tau_{\text{hb}}} \cdot \frac{1}{1 + \exp(\frac{(V_{\text{offhb}} - V)}{V_{\text{slohb}}})}$$

$$h_\infty = \frac{\alpha_h}{\alpha_h + \beta_h}$$

$$\tau_h = \frac{1}{\alpha_h + \beta_h}$$

$V_{\text{offma}} = -27$ mV, $V_{\text{offmb}} = -75$ mV, $V_{\text{offha}} = -13$ mV, $V_{\text{offhb}} = -15$ mV, $V_{\text{sloma}} = 3.8$ mV, $V_{\text{slomb}} = 17$ mV, $V_{\text{sloha}} = 50$ mV, $V_{\text{slohb}} = 28$ mV, $\tau_{\text{ma}} = 18.18$ ms, $\tau_{\text{mb}} = 1.06$ ms, $\tau_{\text{ha}} = 2188.18$ ms, $\tau_{\text{hb}} = 153.85$ ms, $\bar{g}_s = 0.000838$ S/cm^2, $\bar{g}_{a_1} = 0.000977$

S/cm^2, $N_m = 2$, $N_h = 1$

Low-voltage-activated Ca^{2+} current, I_{CaLVA}

$$m_\infty = \frac{1}{1+\exp(\frac{V_{\mathrm{offm}}-V}{V_{\mathrm{slom}}})}$$

$$h_\infty = \frac{1}{1+\exp(-\frac{V_{\mathrm{offh}}-V}{V_{\mathrm{sloh}}})}$$

$$\tau_m = \tau_{\mathrm{mmin}} + \frac{\tau_{\mathrm{mdiff}}}{T_{\mathrm{adj}}\left(1+\exp(-\frac{V_{\mathrm{offmt}}-V}{V_{\mathrm{slomt}}})\right)}$$

$$\tau_h = \tau_{\mathrm{hmin}} + \frac{\tau_{\mathrm{hdiff}}}{T_{\mathrm{adj}}\left(1+\exp(-\frac{V_{\mathrm{offht}}-V}{V_{\mathrm{sloht}}})\right)}$$

$V_{\mathrm{offma}} = -40.0$ mV, $V_{\mathrm{offmt}} = -35.0$ mV, $V_{\mathrm{offha}} = -90.0$ mV, $V_{\mathrm{offht}} = -50.0$ mV, $V_{\mathrm{sloma}} = 6.0$ mV, $V_{\mathrm{slomt}} = 5.0$ mV, $V_{\mathrm{sloha}} = 6.4$ mV, $V_{\mathrm{sloht}} = 7.0$ mV, $\tau_{\mathrm{mmin}} = 5.0$ ms, $\tau_{\mathrm{mdiff}} = 20.0$ ms, $\tau_{\mathrm{hmin}} = 20.0$ ms, $\tau_{\mathrm{hdiff}} = 50.0$ ms, $\bar{g}_s = 0.00311$ S/cm^2, $\bar{g}_{a_1} = 0.000487$ S/cm^2, $N_m = 2$, $N_h = 1$

Small-conductance Ca^{2+}-activated K^+ current, I_{SK}

$$m_\infty = \frac{1}{1+\left(\frac{[\mathrm{Ca}^{2+}]_i}{c_{\mathrm{off}}}\right)^{-c_{\mathrm{slo}}}}$$

$c_{\mathrm{off}} = 0.00043$ mM, $c_{\mathrm{slo}} = 4.8$, $\bar{g}_s = 0.0479$ S/cm^2, $\bar{g}_{a_0} = 0.000231$ S/cm^2, $\bar{g}_{a_1} = 0.00365$ S/cm^2, $N_m = 1$, $N_h = 1$

Leak current, I_{leak}
$E = -90$ mV, $\bar{g}_s = 0.000078$ S/cm^2, $\bar{g}_{a_0} = 0.0000592$ S/cm^2, $\bar{g}_{a_1} = 0.0000675$ S/cm^2, $\bar{g}_b = 0.0000256$ S/cm^2, $N_m = 0$, $N_h = 0$

Intracellular $[Ca^{2+}]$ dynamics
The intracellular Ca^{2+} concentration follows Equation S1 with the following model parameters: $\gamma_s = 0.0005$, $\gamma_{a_0} = 0.0347$, $\gamma_{a_1} = 0.0005$, $\tau_{\mathrm{decay},s} = 488$ ms, $\tau_{\mathrm{decay},a_0} = 142$ ms, $\tau_{\mathrm{decay},a_1} = 95.4$ ms, $d = 0.1$ µm, $c_{\mathrm{min}} = 10^{-4}$ mM

Temperature adjustment factor: $T_{\mathrm{adj}} = 2.3^{\frac{34-21}{10}}$

S1.1.4 The synapse models

Our model for synaptic connections and network connectivity is taken from Hay and Segev, 2015. Each neuron receives 10000 glutamatergic and 2500 GABAergic thalamocortical and corticocortical inputs from neurons outside the modeled network. The timings of these background inputs follow stationary (in network gain experiments) or non-stationary (in oscillation experiments, see below) Poisson statistics, where the (average) event rate is 0.72 Hz for glutamatergic inputs and 7.0 Hz for GABAergic inputs (Hay and Segev, 2015), unless otherwise stated. In addition, the model neurons are randomly connected with glutamatergic synapses (5 synaptic contacts at the receiving neuron) to each other such that the probability for a pair of neurons being reciprocally connected is 0.06 and the probability for them being unidirectionally connected is 0.13 (Hay and Segev, 2015). The glutamatergic synapses conduct AMPA- and NMDA-type currents, of which the NMDA-type currents are voltage-gated as follows (Jahr and Stevens, 1990):

$$g_{\mathrm{NMDA}}(V) = \frac{g_{\mathrm{max,glut}}}{1+\exp(-0.062\frac{1}{\mathrm{mV}}\times V)/3.57}.$$

All three types of synaptic currents have a rising-falling exponential form, which can be described by two state variables, A and B as follows:

$$\frac{dA}{dt} = -\frac{A}{\tau_A} + \sum_{i=1}^{N_{act}} \delta(t - t_{syn}^{(i)})$$

$$\frac{dB}{dt} = -\frac{B}{\tau_B} + \sum_{i=1}^{N_{act}} \delta(t - t_{syn}^{(i)}),$$

where the terms $t_{act}^{(i)}$, $i = 1, \ldots, N_{act}$ refer to the synapse activation times, i.e., timings of the pre-synaptic spikes that induced a synaptic release. The synaptic conductances are calculated as

$$\begin{cases} g_{glut}(t) = g_{\mathrm{max,glut}}(B_{\mathrm{AMPA}}(t) - A_{\mathrm{AMPA}}(t)) + g_{\mathrm{NMDA}}(V(t))(B_{\mathrm{NMDA}}(t) - A_{\mathrm{NMDA}}(t)) \\ g_{\mathrm{GABA}}(t) = g_{\mathrm{max,GABA}}(B_{\mathrm{GABA}}(t) - A_{\mathrm{GABA}}(t)) \end{cases}$$

The background synapses are subject to a probabilistic short-term depression rule, which is modeled using the variable U that obeys the following dynamics (Fuhrmann et al., 2002):

$$\frac{dU}{dt} = \frac{1-U}{\tau_{rec}} - U_{SE}U \sum_{i=1}^{N_{act}} \delta(t - t_{act}^{(i)}),$$

and the probability of release at a time of a presynaptic spike $t_{syn}^{(i)}$ (i.e., $P(t_{syn}^{(i)} \in \{t_{act}^{(i)} | i = 1, \ldots, N_{act}\})$) depends on the variable $U \in [0, 1]$ as

$$P_r(t_{syn}^{(i)}) = U_{SE}U(t_{syn}^{(i)}).$$

In the intra-network synapses, by contrast, are non-depressing ($U = 1$) as in Hay and Segev, 2015. The model parameters concerning the kinetics of the synaptic currents are as follows: $\tau_{A,\mathrm{AMPA}} = 0.3$ ms, $\tau_{B,\mathrm{AMPA}} = 3.0$ ms, $\tau_{A,\mathrm{NMDA}} = 2.0$ ms, $\tau_{B,\mathrm{NMDA}} = 65$ ms, $\tau_{A,\mathrm{GABA}} = 1.0$ ms, and $\tau_{B,\mathrm{GABA}} = 20$ ms.

The maximal conductances of the synaptic currents were set $g_{\mathrm{max,glut}} = 0.00039$ μS and $g_{\mathrm{max,GABA}} = 0.0006$ μS. These values were changed from Hay and Segev, 2015 (where they were $g_{\mathrm{max,glut}} = 0.0004$ μS and $g_{\mathrm{max,GABA}} = 0.001$ μS) due to an error in their synapse activation code: in the scripts implemented in Hay and Segev, 2015, the synaptic depression variable U (P_v in their code) was updated at each time of presynaptic spike, regardless whether it caused a synaptic release or not. In this work, we optimized the variables $g_{\mathrm{max,glut}}$ and $g_{\mathrm{max,GABA}}$ using a grid-search approach to make our model neuron produce (in single-cell simulations) as similar spiking behaviour as possible to the firing behaviour of the model neuron of Hay and Segev, 2015. This was done by minimizing the difference between the numbers of spikes in network simulations where the activation rates of background synapses were varied from -60% to +60% in increments of 10% and the corresponding numbers in simulations of the network model of Hay and Segev, 2015. The reason for the large difference in the values of $g_{\mathrm{max,GABA}}$ compared to that in the values of $g_{\mathrm{max,glut}}$ is that the GABAergic synapses were activated much more frequently (7.0 Hz vs. 0.72 Hz), and thus the probability of synaptic release is constantly smaller in the GABAergic synapses than in the glutamatergic synapses.

After the maximal conductances of the synaptic currents were fixed based on single-cell simulations, we set the intra-network synaptic conductances as $g_{\mathrm{max,glut},E\to E} = c_{gEE} g_{\mathrm{max,glut}}$, where the coefficient $c_{gEE} = 1.07$ was fitted to make the neurons in the interconnected network produce the same firing rate (4.66 Hz) as the original network (Hay and Segev, 2015).

S1.1.5 The excitatory-inhibitory network model

In this section, we extended the L5PC network model by adding a population of inhibitory interneurons that communicated with the L5PC population. We did not aim at providing a network model that is biologically detailed in all aspects, as that would require following all the steps made in Markram et al., 2015. Instead, our goal was to incorporate the interneurons in a way that is both computationally feasible and affects the L5PC network activity in a robust manner that is in line with previous computational studies. To prevent large increase in the computational load of the network model, we used the single-compartment fast-spiking basket cell model as presented in Pospischil et al., 2008. This model includes the passive leak current $I_l = g_l(V - E_l)$ and the Hodgkin-Huxley-type Na^+ and K^+ currents, $I_{Na} = g_{Na}m^3h(V - E_{Na})$ and $I_K = g_K n^4(V - E_K)$, whose activation variables (m and n) and inactivation variable (h) obey the following dynamics (Pospischil et al., 2008):

$$\frac{dm}{dt} = \alpha_m(V)(1-m) - \beta_m(V)m$$

$$\frac{dh}{dt} = \alpha_h(V)(1-h) - \beta_h(V)h$$

$$\frac{dn}{dt} = \alpha_n(V)(1-n) - \beta_n(V)n$$

$$\alpha_m(V) = \frac{-0.32(V - V_T - 13\ \mathrm{mV})}{\exp(-(V - V_T - 13\ \mathrm{mV})/4\ \mathrm{mV}) - 1}$$

$$\beta_m(V) = \frac{0.28(V - V_T - 40\ \mathrm{mV})}{\exp((V - V_T - 40\ \mathrm{mV})/5\ \mathrm{mV}) - 1}$$

$$\alpha_h(V) = 0.128 \exp(-(V - V_T - 17\ \mathrm{mV})/18\ \mathrm{mV})$$

$$\beta_h(V) = \frac{4}{1 + \exp(-(V - V_T - 40\ \mathrm{mV})/5\ \mathrm{mV})}$$

$$\alpha_n(V) = \frac{-0.32(V - V_T - 15\ \mathrm{mV})}{\exp(-(V - V_T - 15\ \mathrm{mV})/5\ \mathrm{mV}) - 1}$$

$$\beta_n(V) = 0.5 \exp(-(V - V_T - 10\ \mathrm{mV})/40\ \mathrm{mV}),$$

where $g_{Na} = 0.05$ S/cm^2, $E_{Na} = 50$ mV, $g_K = 0.005$ S/cm^2, E_K = -90 mV, and V_T = -63 mV. The shape of the basket cell was a cylinder with both length and diameter 67 μm. The membrane capacitance was 1.0 μS/cm^2 and the passive properties were $g_l = 0.00015$ S/cm^2 and E_l = -70 mV.

The basket cells, similarly to the L5PCs, received 10000 glutamatergic and 2500 GABAergic background synaptic inputs that had the same temporal activation properties as the L5PCs. The basket cells were randomly connected to each other

with a probability 0.06 and to L5PCs with a probability 0.04 (E→I) or 0.09 (I→E) — these values were estimated as averages of layer V basket cell connectivity data in Figure 7 of Markram et al., 2015, and unlike for E→E connections, no distinction was made between probabilities of reciprocal vs. unidirectional connections. In addition, the basket cells were connected to each other with gap junctions such that the probability of connection was 1.0 (gap junction always existed) between basket cells that were reciprocally connected to each other by chemical synapses, 0.37 between basket cells that were connected in a unidirectional way, and 0.2 between unconnected basket cells (values from Table 1 in Galarreta and Hestrin, 2002). No gap junctions were placed between L5PCs nor between an L5PC and a basket cell. For compatibility with the model of Hay and Segev, 2015 where the GABAergic background synapses were uniformly distributed along the L5PC morphology, the basket cell projections to L5PC were also uniformly distributed along the L5PCs, although these projections are typically concentrated at perisomatic compartments and proximal dendrites (Somogyi et al., 1998).

The AMPA, NMDA and GABA conductances received by the basket cells were scaled up from the corresponding values in the L5PC network model to make the basket cells fire spontaneously. Experimental studies suggest a very variable firing rate of the basket cell population: estimates of the spontaneous firing rate include 2.1 Hz (visual cortex, *in vivo*) (Atallah et al., 2012), 4.9 Hz (dysplastic cortex, *ex vivo*, in an "environment that mildly enhanced firing of the neurons") (Zhou and Roper, 2010), 5.5 Hz (auditory cortex, *in vivo*) (Moore and Wehr, 2013), 9.3 Hz (Chen et al., 2015) (auditory cortex, *in vivo*), and 12.4 Hz (medial entorhinal cortex, *in vivo*) (Buetfering et al., 2014).

To test the validity of our results in multiple conditions, we scaled up the synaptic conductances using three different coefficients, namely, $c_{gI} = 2.0$, 6.0, and 12.0. In addition, we run our simulations using different degrees of synchronization, mediated by three different values of gap junction conductance g_{GJ}, namely 2e-5 μS (weak), 0.0002 μS (moderate, see Galarreta and Hestrin, 2002), and 0.002 μS (strong). For any combination of these values that we applied, we mildly upscaled the excitatory-to-excitatory synaptic conductances (multiplied by c_{gEE}) in the L5PCs in order to produce the same network firing frequency as produced by the control L5PC-only network. The values of c_{gEE} are shown in Table S1. In Figure S1, we illustrate the network dynamics in excitatory-inhibitory networks with different combinations of these chemical and electrical synapse conductances. The smallest coefficient $c_{gI} = 2.0$ resulted in few spikes in the inhibitory population — when gap junctions were strong, the spiking of the inhibitory population was even sparser due to the larger inertia that these junctions impose. This was reflected also in the power spectra, which showed relatively low power in both cases but especially in the case of strong gap junctions ($g_{GJ} = 0.002$ μS). By contrast, when the synaptic conductances at the inhibitory neurons were strong ($c_{gI} = 12.0$), the spiking in the inhibitory population was dense (5.7 or 6.7 spikes/second/neuron, when $g_{GJ} =$ 2e-5 or 0.002 μS, respectively). The effect of the stronger gap junctions can be seen in both the spike trains of the inhibitory population as an increased synchrony and in the power spectra of the inhibitory population as an increased beta power. As expected, the intermediate coefficient $c_{gI} = 6.0$ with moderate gap junctions $g_{GJ} = 0.0002$ resulted in intermediate spiking activity in the inhibitory population (4.6 spikes/second/neuron). The effect of the neuronal activity in the inhibitory population on the activity of the excitatory population depends both on the overall level of activity as well as synchronization in the inhibitory population.

Table S1: Coefficients for excitatory-to-excitatory synaptic conductances (c_{gEE}) in excitatory-inhibitory networks that resulted in the same number of spikes as in the L5PC-only network (where c_{gEE} was 1.07). These values were obtained using grid-search method and interpolation by simulating the network activity for each combination of g_{GJ} and c_{gI} separately using several (9 – 14) values of coefficient c_{gEE} and N = 10–20 repetitions for each value of c_{gEE}.

g_{GJ} (μS) \ c_{gI}	2.0	4.0	6.0	8.0	10.0	12.0
0.00002	1.11	1.41	1.59	1.64	1.69	1.75
0.0002	1.10	1.39	1.59	1.63	1.68	1.74
0.002	1.08	1.28	1.67	1.77	1.83	1.9

S1.2 Representation of genetic alterations in the L5PC model

The main body of our results is based on models of common variants of SCZ-associated genes, which were constructed based on GWAS results and functional genomics data from the literature. As done previously (Mäki-Marttunen et al., 2016), we estimated the impact of functional variants of SCZ-associated ion channel and Ca^{2+} transporter-encoding genes by downscaling the effects of genetic variants that have larger phenotypic consequences. We first chose the set of genes of interest based on the SNP-wise p-value data of Ripke et al., 2014, and searched the literature for variants of these genes and their effects on cell electrophysiology. We restricted our survey on genes that are likely to be expressed in L5PCs and on variants whose effects could be implemented as a parameter change in our single-cell L5PC model (Hay et al., 2011). We found 32 studies reporting variants of nine ion-channel or Ca^{2+} transporter-encoding genes: *CACNA1C*, *CACNA1D*, *CACNB2*, *CACNA1I*, *ATP2A2*, *ATP2B2*, *SCN1A*, *HCN1*, and *KCNB1* (see Section S1.2.1 below). These studies and the effects of the underlying variants on model parameters are listed in Table S2. The underlying variants could be directly implemented in our L5PC model. However, the effects of most model variants on the L5PC excitability were large, which is not expected from common variants. Therefore, following the procedure of Mäki-Marttunen et al., 2016, we imposed conditions on how much the neuron responses (to predefined stimuli) were allowed to vary, and scaled down the parameter changes related to each of the model variants until these conditions were met. In practice, each change of parameter that was related to a considered variant as presented in Table S2 was multiplied (on linear or logarithmic scale, depending on the type of the underlying parameter) by a scaling parameter $c = c_{\text{thresh}}$, where the parameter c_{thresh} was determined as the largest factor $c \in [0, 2]$ for which the scaling conditions 1–5 concerning single-neuron firing behaviour (see Section S1.2.2 below) were met.

This gave us a library of small-effect model variants (Table S3), which we then further downscaled with fixed factors $\epsilon \in \mathbb{R}$ and employed as models for effects of common variants of the underlying genes on L5PC electrophysiological properties.

In this work, we present simulation data from the model networks populated with variants downscaled as $c = \epsilon c_{\text{thresh}}$, where $\epsilon \in \{\frac{1}{2}, \frac{1}{4}, -\frac{1}{4}, -\frac{1}{2}\}$ is a downscaling parameter. Variants with $\epsilon = \frac{1}{2}$ and $\epsilon = \frac{1}{4}$ mean that the variant effects on model parameters are a half or a quarter, respectively, of those of the threshold variants — these variants are therefore confirmed to obey the abovementioned scaling conditions. In addition, we consider the variants $\epsilon = -\frac{1}{2}$ and $\epsilon = -\frac{1}{4}$, which represent parameter changes that are opposite to those of $\epsilon = \frac{1}{2}$ and $\epsilon = \frac{1}{4}$ variants. These model variants do not necessarily obey the scaling conditions, but due to the properties of the underlying system (the differential equations are continuously differentiable with respect to all considered model parameters), small enough changes in the parameters behave in a fairly linear manner — this is implicitly shown by our results. The control network can be considered a model variant with zero-magnitude parameter changes ($\epsilon = 0$). In parallel with this SNP-like variant-based analysis, we consider the effects of altered expression of ion channel or Ca^{2+} transporter-encoding genes in SCZ patients. Both approaches are constrained by data available on the expression of these genes in L5PCs (see Methods).

S1.2.1 Functional genomics literature review

We searched through the literature on functional genomics for genes *CACNA1C*, *CACNA1D*, *CACNB2*, *CACNA1I*, *ATP2A2*, *ATP2B2*, *SCN1A*, *HCN1*, and *KCNB1* to find data on how genetic variations change the ion channel behavior or intracellular Ca^{2+} dynamics. Due to lack of data reported for a single animal and cell type, we included studies performed in various animal species and across different tissues. We concentrated on studies that fulfilled the following conditions:

- The study applied a genetic variant of one of the genes of interest.
- The properties of the cell expressing the gene variant were studied using electrophysiology or Ca^{2+} imaging.
- The deviation between the variant cell property and the control cell property could be implemented in the applied L5PC model as a change of model parameter values.
- The observed effect of the gene variant was not solely on the expression or ion channel density level.

The last condition, which ruled out studies where the effect was only shown on channel density, was set due to the multitude of pathways that may contribute to such an effect (Rosati and McKinnon, 2004). By contrast, the effects on channel kinetics (activation and inactivation threshold potentials, sensitivity to membrane potential, and opening/closing time constants) were expected to be more straightforwardly dependent on the way these channels are genetically coded. Table S2 lists the relevant data from all studies (Kudrnac et al., 2009; Depil et al., 2011; Hohaus et al., 2005; Stary et al., 2008; Tang et al., 2004; Tan et al., 2011; Bock et al., 2011; Zhang et al., 2011; Pérez-Alvarez et al., 2011; Pinggera et al., 2015; Azizan et al., 2013; Lieb et al., 2012; Cordeiro et al., 2009; Massa et al., 1995; Link et al., 2009; Hu et al., 2010; Murbartián et al., 2004; Gomora et al., 2002; Ji et al., 2000; Fakira et al., 2012; Empson et al., 2010; Ficarella et al., 2007; Giacomello et al., 2011; Cestèle et al., 2008; Vanmolkot et al., 2007; Volkers et al., 2011; Cestèle et al., 2013; Mantegazza et al., 2005; Ishii et al., 2007; Lesso and Li, 2003; Wemhöner et al., 2015; Bocksteins et al., 2011) that were found to obey the above conditions.

Some of the studies cited in Table S2 regarded several variant types, and in these cases, the range of possible effects on model parameters is considered. If the range spanned both increasing and decreasing effects, the analyses were carried out for both endpoints of the range, otherwise only the maximal deviation from the control value was considered. Also, in case one of the endpoints of the range was very close to the control value, namely, at a distance less than 1 mV or less than 10% of the distance between control value and the other endpoint, only the endpoint with the larger deviation was considered.

Table S2: **Table of the genetic variants used in this study.** The first column of the table shows the gene whose variant was studied in the named reference. The second and third columns show the current species and the model parameters that are affected by the variant, "offm" and "offh" meaning the mid-points of activation and inactivation, respectively, "slom" and "sloh" their slopes, and "taum" and "tauh" their time constants. For brevity, semicolons differentiate multiple parameter changes in a single row. The parameter names may refer to multiple model parameters: For example, for HVA Ca^{2+} currents, a change in "offm" means a concurrent change in parameters V_{offma} and V_{offmb}, while "offh" refers to parameters V_{offha} and V_{offhb}, "slom" to V_{sloma} and V_{slomb}, "sloh" to V_{sloha} and V_{slohb}, "taum" to τ_{ma} and τ_{mb}, and "tauh" to τ_{ha} and τ_{hb}. See model equations in Supplementary material, Text S2 for details. The fourth column shows the direction and magnitude of the effect, ±x mV referring to a shift of the middle-point of the (in)activation curve by an absolute number of millivolts, and ±x% referring to a percentual change in the underlying quantity. In many cases, several variants were considered in a single study: Here, they are categorized by the type of the variant when necessary (e.g., in Kudrnac et al., 2009 several variants of four loci, of which three were in pore-lining IS6 segment and two in bundle-crossing region of segment IIS6, were considered, and the variants are here categorized according to the segment they acted on). The fifth column names the type of variant used, while the sixth column shows the cell type in which the effects were measured.

Gene		Current	Parameter	Effect	Type of variant	Cell type
CACNA1C	Kudrnac et al., 2009	I_{CaHVA}	offm; offh	-25.9..-1.4mV; -27.0..-3.8mV	L429T, L434T, S435T, S435A, S435P	TSA201
CACNA1C	Kudrnac et al., 2009	I_{CaHVA}	offm; offh	-37.3..-9.7mV; -30.0..-11.8mV	L779T, I781T, I781P	TSA201
CACNA1C	Depil et al., 2011	I_{CaHVA}	offm; offh slom; sloh	-31.4..+7.0mV; -28.5..+16.3mV -15..+45%; -28%..+38%	G432X, A780X, G1193X, A1503X	TSA201
CACNA1C	Hohaus et al., 2005	I_{CaHVA}	offm slom	-38.5..+12.9mV -54..+56%	I781X, C769P, G770P, N771P, I773P F778P, L779P, A780P, A782P, V783P	TSA201
CACNA1C	Stary et al., 2008	I_{CaHVA}	offm; offh slom	-27.8..+8.7mV; -19.1..+4.7mV -11%..+14%	I781T, N785A, N785G, N785L	TSA201
CACNA1C	Tang et al., 2004	I_{CaHVA}	offm; offh sloh	-11.2..+1.0mV; -3.1..-0.3mV +3%..+24%	Splice variants a1C77-A, -B, -C, and -D	TSA201
CACNA1D	Tan et al., 2011 Bock et al., 2011	I_{CaHVA}	offm; offh slom; sloh tauh	-10.9..-8.5mV; -3.0..+3.5mV -27..-13%; -12..-19% +25%	Splice variant 42A	TSA201 / HEK293
CACNA1D	Tan et al., 2011 Bock et al., 2011	I_{CaHVA}	offm; offh slom; sloh tauh	-10.6..+3.4mV; -5.3..+1.2mV -20..+12%; -34..-8% -28%	Splice variant 43S	TSA201 / HEK293
CACNA1D	Zhang et al., 2011 Pérez-Alvarez et al., 2011	I_{CaHVA}	offm slom; tauh	+3.5..+6.6mV -25..+19%; -50..+12%	Homozygous knockout	AV-node / chromaffin cells
CACNA1D	Pinggera et al., 2015	I_{CaHVA}	offm; offh slom; sloh	-9.8mV; -15.4mV -20%; sloh	A749G	TSA201
CACNA1D	Azizan et al., 2013	I_{CaHVA}	offm; offh slom; sloh tauh	-24.2..+6.1mV; -14.5..-3.6mV -30..+24%; -28%..+28% +43%..+252%	V259D, I750M, P1336R	TSA201
CACNA1D	Lieb et al., 2012	I_{CaHVA}	offm slom; tauh	-17.8..-13.1mV -19..-0%; -23%..+31%	rCav1.3scg variant and mutants 7M2K, S244G, V1104A, and A2075V	TSA201
CACNB2	Cordeiro et al., 2009	I_{CaHVA}	offh; sloh	-5.2mV; -31%	T11I	TSA201
CACNB2	Massa et al., 1995	I_{CaHVA}	taum	+70%	A1B2 vs A1 alone	HEK293
CACNB2	Link et al., 2009	I_{CaHVA}	offm; offh taum; tauh	-4.9..+4.9mV; -5.1..+5.1mV -40%..+68%; -40%..+66%	Splice variants N1, N3, N4, and N5	HEK293
CACNB2	Hu et al., 2010	I_{CaHVA}	tauh	+26%	D601E	TSA201
CACNA1I	Murbartián et al., 2004	I_{CaLVA}	offm; offh taum; tauh	-0.2..+1.3mV; -0.5..+1.6mV -13..+45%; -20..+8%	Alternative splicing of exons 9 and 33	HEK293
CACNA1I	Gomora et al., 2002	I_{CaLVA}	offm; offh slom; sloh taum; tauh	-4.3..-1.2mV; -4.4..-1.9mV +5..+14%; -11%..+4% -47%..-15%; -54%..+1%	Truncated cDNAs L4, L6 and L9	HEK293
ATP2A2	Ji et al., 2000	(none)	γ	-30..-40%	Heterozygous knockout	myocytes
ATP2B2	Fakira et al., 2012	(none)	τ_{decay}	+15..+113%	Heterozygous knockout	Purkinje cells
ATP2B2	Empson et al., 2010	(none)	τ_{decay}; c_{min}	+32..+50%; +40%	Homozygous knockout	Purkinje cells
ATP2B2	Ficarella et al., 2007	(none)	τ_{decay}	+53..+345%	G283S, G293S	CHO cells
ATP2B2	Giacomello et al., 2011	(none)	c_{min}	+10%	E584K, T692K	Hair cells
SCN1A	Cestèle et al., 2008	I_{Nat}	offm; offh slom; sloh	-0.3mV; +5.0mV +15%; +23%	Q1489K	Cultured neocortical cells
SCN1A	Vanmolkot et al., 2007	I_{Nat}	offm; offh slom; sloh	+2.8mV; +6.3..+9.6mV -1.6%; +4.2%	L1649Q	TSA201
SCN1A	Volkers et al., 2011	I_{Nat}	offm; offh slom; sloh; tauh	-4.0mV; -5.8mV -8%; +13%; +43..+47%	R859H	TSA201
SCN1A	Volkers et al., 2011	I_{Nat}	offm; offh slom; sloh; tauh	-8.1mV; +2.2mV -3%; -3%; +26..+59%	R865G	TSA201
SCN1A	Cestèle et al., 2013	I_{Nat}	offm; slom; tauh	+6.0mV; +16%; +29%	T1174S	TSA201
SCN1A	Mantegazza et al., 2005	I_{Nat}	offm; offh slom; sloh	+10.0mV; -0.6mV +15%; +14%	M145T	TSA201
HCN1	Ishii et al., 2007	I_h	offh; sloh	-2.1..-26.5mV; -12..-36%	D135W, D135H, D135N	HEK293
HCN1	Lesso and Li, 2003	I_h	offh sloh	-25.9..+17.7mV -40..+3%	E229A, K230A, G231A, M232A, D233A S234A, E235G, V236A, Y237A, EVY235-237DDD	Oocytes
HCN1	Wemhöner et al., 2015	I_h	offh; tauh	+2.4..+3.9mV; -12..-0%	WAG-HCN1, WAG-HCN1 + HCN1 co-expression	Oocytes
KCNB1	Bocksteins et al., 2011	I_{Kp}	offm; offh slom; sloh taum; tauh	+5mV; +3mV +11%; -14% -50%; -47%	T203K	HEK293
KCNB1	Bocksteins et al., 2011	I_{Kp}	offm; offh slom taum; tauh	+1mV; -6mV +22% -11%; -13%	T203D	HEK293
KCNB1	Bocksteins et al., 2011	I_{Kp}	offm; offh slom taum; tauh	+6mV; -8mV +33% -50%; -13%	S347K	HEK293
KCNB1	Bocksteins et al., 2011	I_{Kp}	offm; offh slom; sloh taum; tauh	-28mV; -27mV +11%; -29% +13%; +127%	S347D	HEK293
KCNB1	Bocksteins et al., 2011	I_{Kp}	offm; offh slom taum; tauh	+14mV; -21mV +100% -61%; +20%	T203W	HEK293
KCNB1	Bocksteins et al., 2011	I_{Kp}	offm; offh slom; sloh taum; tauh	-13mV; -13mV +33%; -29% -5%; +413%	S347W	HEK293

S1.2.2 Scaling of gene variants

As SCZ is a polygenic disorder, it has been proposed that the disorder will not be induced by any of the SCZ-related SNPs alone, but only when sufficiently many of them are represented. This paradigm was used in this study in a similar fashion as in Mäki-Marttunen et al., 2016. If the model variants described in Table S2 altered the neural response or cardiac pacemaking too dramatically (see conditions 1–5), the genetic effect was scaled down so that there were no large discrepancies between the control neuron and the mutant with the downscaled variant. This approach was used in order to simulate the SCZ-related SNP effects, many of which are known to be subtle (cf. Lee et al., 2012) in contrast to the large phenotypic effects caused by the model variants of Table S2.

To scale down the model variants of Table S2 when implemented in the L5PC models, we followed the downscaling procedure as presented in Mäki-Marttunen et al., 2016. The downscaling criteria were the following:
(1) Exactly 4 spikes should be induced as a response to somatic square-current injection of 0.696 nA $\times$ 150 ms,
(2) Exactly 1 spike should be induced as a response to a distal (620 µm from soma) alpha-shaped synaptic conductance (time constant 5 ms, max. amplitude 0.0612 µS),
(3) Exactly 2 spikes should be induced as a response to a combined stimulus of somatic square-current injection (1.137 nA $\times$ 10 ms) and distal synaptic conductance (time constant 5 ms, max. amplitude 0.100 µS, applied 5ms after the somatic pulse),
(4) The integrated difference between the f-I curves of the considered neuron and the control neuron should not be more than 10% of the integral of the control neuron f-I curve, and
(5) The membrane-potential limit cycle should not be too different from the control neuron limit cycle ($d_{cc}(lc_1, lc_2) \leq 600$, see Mäki-Marttunen et al., 2016 for the definition of the metric d_{cc}).

The conditions 1–3 restrict the magnitudes of short-time responses of the neuron, while the conditions 4–5 concern continuous, steady-state firing as a response to somatic DC stimulus. The above-mentioned amplitudes were chosen such that the control neuron most stably produces the named numbers of spikes with the default parameters — most stably in the sense that an equal change in current amplitude on logarithmic scale is required in order to produce one spike more or to produce one spike less.

In case one or more of the conditions 1–5 were violated when the cell with the considered model variant was simulated, the effect was scaled down — all parameters in proportion — to a fraction $c < 1$ of the original effect where the violation is for the first time observed. These threshold effect parameters c_{thresh} are listed in Table S3 for each model variant together with the corresponding parameter changes, and the model variants that were used in Figures 1–2 are highlighted. As we do not know how small a parameter change should be to correspond to a small gene-variant effect, we consider model variants with different scalings where the threshold effect parameter c_{thresh} is multiplied with another parameter $\epsilon < 1$. In this work, we consider the scaling parameter values $\epsilon = \frac{1}{2}$ and $\frac{1}{4}$, and we also display the effects of the corresponding opposite model variants $\epsilon = -\frac{1}{2}$ and $-\frac{1}{4}$.

Table S3: **Table for the effects of the genetic variants on model parameters.** The first column names the gene and the study in which the gene variant was analyzed. The second column shows the effect of the variant on the model parameters, "offm" and "offh" meaning the mid-points of activation and inactivation, respectively, "slom" and "sloh" their slopes, and "taum" and "tauh" their time constants. The third column shows the threshold scaling parameter of the variant. all models. The rows separated by horizontal lines correspond to different entries of Table S2: If the corresponding study showed a large range of effects on single model parameters, the endpoints of such ranges are here treated as different variants that are downscaled independently of each other. Asterisks (*) mark the variants used in Figures 1 and 2.

Gene	Parameter changes	Scaling parameter	
CACNA1C Kudrnac et al., 2009	$V_{\text{offm}*,\text{CaHVA}}$: -25.9 mV; $V_{\text{offh}*,\text{CaHVA}}$: -27.0 mV	$c_{\text{thresh}} = 0.094$	
CACNA1C Kudrnac et al., 2009	$V_{\text{offm}*,\text{CaHVA}}$: -37.3 mV; $V_{\text{offh}*,\text{CaHVA}}$: -30.0 mV	$c_{\text{thresh}} = 0.060$	
CACNA1C Depil et al., 2011	$V_{\text{offm}*,\text{CaHVA}}$: -31.4 mV; $V_{\text{slom}*,\text{CaHVA}}$: *0.85; $V_{\text{offh}*,\text{CaHVA}}$: -28.5 mV; $V_{\text{sloh}*,\text{CaHVA}}$: *0.72	$c_{\text{thresh}} = 0.061$	
	$V_{\text{offm}*,\text{CaHVA}}$: +7.0 mV; $V_{\text{slom}*,\text{CaHVA}}$: *0.85; $V_{\text{offh}*,\text{CaHVA}}$: -28.5 mV; $V_{\text{sloh}*,\text{CaHVA}}$: *0.72	$c_{\text{thresh}} = 0.141$	
	$V_{\text{offm}*,\text{CaHVA}}$: -31.4 mV; $V_{\text{slom}*,\text{CaHVA}}$: *1.45; $V_{\text{offh}*,\text{CaHVA}}$: -28.5 mV; $V_{\text{sloh}*,\text{CaHVA}}$: *0.72	$c_{\text{thresh}} = 0.071$	
	$V_{\text{offm}*,\text{CaHVA}}$: +7.0 mV; $V_{\text{slom}*,\text{CaHVA}}$: *1.45; $V_{\text{offh}*,\text{CaHVA}}$: -28.5 mV; $V_{\text{sloh}*,\text{CaHVA}}$: *0.72	$c_{\text{thresh}} = 0.107$	
	$V_{\text{offm}*,\text{CaHVA}}$: -31.4 mV; $V_{\text{slom}*,\text{CaHVA}}$: *0.85; $V_{\text{offh}*,\text{CaHVA}}$: +16.3 mV; $V_{\text{sloh}*,\text{CaHVA}}$: *0.72	$c_{\text{thresh}} = 0.044$	
	$V_{\text{offm}*,\text{CaHVA}}$: +7.0 mV; $V_{\text{slom}*,\text{CaHVA}}$: *0.85; $V_{\text{offh}*,\text{CaHVA}}$: +16.3 mV; $V_{\text{sloh}*,\text{CaHVA}}$: *0.72	$c_{\text{thresh}} = 0.693$	
	$V_{\text{offm}*,\text{CaHVA}}$: -31.4 mV; $V_{\text{slom}*,\text{CaHVA}}$: *1.45; $V_{\text{offh}*,\text{CaHVA}}$: +16.3 mV; $V_{\text{sloh}*,\text{CaHVA}}$: *0.72	$c_{\text{thresh}} = 0.048$	
	$V_{\text{offm}*,\text{CaHVA}}$: +7.0 mV; $V_{\text{slom}*,\text{CaHVA}}$: *1.45; $V_{\text{offh}*,\text{CaHVA}}$: +16.3 mV; $V_{\text{sloh}*,\text{CaHVA}}$: *0.72	$c_{\text{thresh}} = 0.359$	
	$V_{\text{offm}*,\text{CaHVA}}$: -31.4 mV; $V_{\text{slom}*,\text{CaHVA}}$: *0.85; $V_{\text{offh}*,\text{CaHVA}}$: -28.5 mV; $V_{\text{sloh}*,\text{CaHVA}}$: *1.38	$c_{\text{thresh}} = 0.082$	
	$V_{\text{offm}*,\text{CaHVA}}$: +7.0 mV; $V_{\text{slom}*,\text{CaHVA}}$: *0.85; $V_{\text{offh}*,\text{CaHVA}}$: -28.5 mV; $V_{\text{sloh}*,\text{CaHVA}}$: *1.38	$c_{\text{thresh}} = 0.081$	
	$V_{\text{offm}*,\text{CaHVA}}$: -31.4 mV; $V_{\text{slom}*,\text{CaHVA}}$: *1.45; $V_{\text{offh}*,\text{CaHVA}}$: -28.5 mV; $V_{\text{sloh}*,\text{CaHVA}}$: *1.38	$c_{\text{thresh}} = 0.103$	
	$V_{\text{offm}*,\text{CaHVA}}$: +7.0 mV; $V_{\text{slom}*,\text{CaHVA}}$: *1.45; $V_{\text{offh}*,\text{CaHVA}}$: -28.5 mV; $V_{\text{sloh}*,\text{CaHVA}}$: *1.38	$c_{\text{thresh}} = 0.068$	
	$V_{\text{offm}*,\text{CaHVA}}$: -31.4 mV; $V_{\text{slom}*,\text{CaHVA}}$: *0.85; $V_{\text{offh}*,\text{CaHVA}}$: +16.3 mV; $V_{\text{sloh}*,\text{CaHVA}}$: *1.38	$c_{\text{thresh}} = 0.054$	
	$V_{\text{offm}*,\text{CaHVA}}$: +7.0 mV; $V_{\text{slom}*,\text{CaHVA}}$: *0.85; $V_{\text{offh}*,\text{CaHVA}}$: +16.3 mV; $V_{\text{sloh}*,\text{CaHVA}}$: *1.38	$c_{\text{thresh}} = 0.219$	
	$V_{\text{offm}*,\text{CaHVA}}$: -31.4 mV; $V_{\text{slom}*,\text{CaHVA}}$: *1.45; $V_{\text{offh}*,\text{CaHVA}}$: +16.3 mV; $V_{\text{sloh}*,\text{CaHVA}}$: *1.38	$c_{\text{thresh}} = 0.061$	
	$V_{\text{offm}*,\text{CaHVA}}$: +7.0 mV; $V_{\text{slom}*,\text{CaHVA}}$: *1.45; $V_{\text{offh}*,\text{CaHVA}}$: +16.3 mV; $V_{\text{sloh}*,\text{CaHVA}}$: *1.38	$c_{\text{thresh}} = 0.142$	
CACNA1C Hohaus et al., 2005	$V_{\text{offm}*,\text{CaHVA}}$: -38.5 mV; $V_{\text{slom}*,\text{CaHVA}}$: *0.46	$c_{\text{thresh}} = 0.040$	
	$V_{\text{offm}*,\text{CaHVA}}$: +12.9 mV; $V_{\text{slom}*,\text{CaHVA}}$: *0.46	$c_{\text{thresh}} = 0.180$	
	$V_{\text{offm}*,\text{CaHVA}}$: -38.5 mV; $V_{\text{slom}*,\text{CaHVA}}$: *1.56	$c_{\text{thresh}} = 0.050$	
	$V_{\text{offm}*,\text{CaHVA}}$: +12.9 mV; $V_{\text{slom}*,\text{CaHVA}}$: *1.56	$c_{\text{thresh}} = 0.091$	
CACNA1C Stary et al., 2008	$V_{\text{offm}*,\text{CaHVA}}$: -27.8 mV; $V_{\text{slom}*,\text{CaHVA}}$: *0.89; $V_{\text{offh}*,\text{CaHVA}}$: -19.1 mV	$c_{\text{thresh}} = 0.075$	
	$V_{\text{offm}*,\text{CaHVA}}$: +8.7 mV; $V_{\text{slom}*,\text{CaHVA}}$: *0.89; $V_{\text{offh}*,\text{CaHVA}}$: -19.1 mV	$c_{\text{thresh}} = 0.107$	
	$V_{\text{offm}*,\text{CaHVA}}$: -27.8 mV; $V_{\text{slom}*,\text{CaHVA}}$: *1.14; $V_{\text{offh}*,\text{CaHVA}}$: -19.1 mV	$c_{\text{thresh}} = 0.081$	
	$V_{\text{offm}*,\text{CaHVA}}$: +8.7 mV; $V_{\text{slom}*,\text{CaHVA}}$: *1.14; $V_{\text{offh}*,\text{CaHVA}}$: -19.1 mV	$c_{\text{thresh}} = 0.096$	
	$V_{\text{offm}*,\text{CaHVA}}$: -27.8 mV; $V_{\text{slom}*,\text{CaHVA}}$: *0.89; $V_{\text{offh}*,\text{CaHVA}}$: +4.7 mV	$c_{\text{thresh}} = 0.059$	
	$V_{\text{offm}*,\text{CaHVA}}$: +8.7 mV; $V_{\text{slom}*,\text{CaHVA}}$: *0.89; $V_{\text{offh}*,\text{CaHVA}}$: +4.7 mV	$c_{\text{thresh}} = 0.201$	
	$V_{\text{offm}*,\text{CaHVA}}$: -27.8 mV; $V_{\text{slom}*,\text{CaHVA}}$: *1.14; $V_{\text{offh}*,\text{CaHVA}}$: +4.7 mV	$c_{\text{thresh}} = 0.063$	
	$V_{\text{offm}*,\text{CaHVA}}$: +8.7 mV; $V_{\text{slom}*,\text{CaHVA}}$: *1.14; $V_{\text{offh}*,\text{CaHVA}}$: +4.7 mV	$c_{\text{thresh}} = 0.164$	
CACNA1C Tang et al., 2004	$V_{\text{offm}*,\text{CaHVA}}$: -11.2 mV; $V_{\text{offh}*,\text{CaHVA}}$: -3.1 mV; $V_{\text{sloh}*,\text{CaHVA}}$: *1.24	$c_{\text{thresh}} = 0.227$	
	$V_{\text{offm}*,\text{CaHVA}}$: +1.0 mV; $V_{\text{offh}*,\text{CaHVA}}$: -3.1 mV; $V_{\text{sloh}*,\text{CaHVA}}$: *1.24	$c_{\text{thresh}} = 0.329$	*
CACNA1D Tan et al., 2011, Bock et al., 2011	$V_{\text{offm}*,\text{CaHVA}}$: -10.9 mV; $V_{\text{slom}*,\text{CaHVA}}$: *0.73; $V_{\text{offh}*,\text{CaHVA}}$: -3.0 mV; $V_{\text{sloh}*,\text{CaHVA}}$: *0.81; $\tau_{\text{h}*,\text{CaHVA}}$: *1.25	$c_{\text{thresh}} = 0.118$	
	$V_{\text{offm}*,\text{CaHVA}}$: -10.9 mV; $V_{\text{slom}*,\text{CaHVA}}$: *0.73; $V_{\text{offh}*,\text{CaHVA}}$: +3.5 mV; $V_{\text{sloh}*,\text{CaHVA}}$: *0.81; $\tau_{\text{h}*,\text{CaHVA}}$: *1.25	$c_{\text{thresh}} = 0.106$	
CACNA1D Tan et al., 2011, Bock et al., 2011	$V_{\text{offm}*,\text{CaHVA}}$: -10.6 mV; $V_{\text{slom}*,\text{CaHVA}}$: *0.8; $V_{\text{offh}*,\text{CaHVA}}$: -5.3 mV; $V_{\text{sloh}*,\text{CaHVA}}$: *0.66; $\tau_{\text{h}*,\text{CaHVA}}$: *0.72	$c_{\text{thresh}} = 0.115$	
	$V_{\text{offm}*,\text{CaHVA}}$: +3.4 mV; $V_{\text{slom}*,\text{CaHVA}}$: *0.8; $V_{\text{offh}*,\text{CaHVA}}$: -5.3 mV; $V_{\text{sloh}*,\text{CaHVA}}$: *0.66; $\tau_{\text{h}*,\text{CaHVA}}$: *0.72	$c_{\text{thresh}} = 1.962$	
	$V_{\text{offm}*,\text{CaHVA}}$: -10.6 mV; $V_{\text{slom}*,\text{CaHVA}}$: *1.12; $V_{\text{offh}*,\text{CaHVA}}$: -5.3 mV; $V_{\text{sloh}*,\text{CaHVA}}$: *0.66; $\tau_{\text{h}*,\text{CaHVA}}$: *0.72	$c_{\text{thresh}} = 0.135$	
	$V_{\text{offm}*,\text{CaHVA}}$: +3.4 mV; $V_{\text{slom}*,\text{CaHVA}}$: *1.12; $V_{\text{offh}*,\text{CaHVA}}$: -5.3 mV; $V_{\text{sloh}*,\text{CaHVA}}$: *0.66; $\tau_{\text{h}*,\text{CaHVA}}$: *0.72	$c_{\text{thresh}} = 0.905$	
	$V_{\text{offm}*,\text{CaHVA}}$: -10.6 mV; $V_{\text{slom}*,\text{CaHVA}}$: *0.8; $V_{\text{offh}*,\text{CaHVA}}$: +1.2 mV; $V_{\text{sloh}*,\text{CaHVA}}$: *0.66; $\tau_{\text{h}*,\text{CaHVA}}$: *0.72	$c_{\text{thresh}} = 0.104$	
	$V_{\text{offm}*,\text{CaHVA}}$: +3.4 mV; $V_{\text{slom}*,\text{CaHVA}}$: *0.8; $V_{\text{offh}*,\text{CaHVA}}$: +1.2 mV; $V_{\text{sloh}*,\text{CaHVA}}$: *0.66; $\tau_{\text{h}*,\text{CaHVA}}$: *0.72	$c_{\text{thresh}} = 0.679$	
	$V_{\text{offm}*,\text{CaHVA}}$: -10.6 mV; $V_{\text{slom}*,\text{CaHVA}}$: *1.12; $V_{\text{offh}*,\text{CaHVA}}$: +1.2 mV; $V_{\text{sloh}*,\text{CaHVA}}$: *0.66; $\tau_{\text{h}*,\text{CaHVA}}$: *0.72	$c_{\text{thresh}} = 0.120$	
	$V_{\text{offm}*,\text{CaHVA}}$: +3.4 mV; $V_{\text{slom}*,\text{CaHVA}}$: *1.12; $V_{\text{offh}*,\text{CaHVA}}$: +1.2 mV; $V_{\text{sloh}*,\text{CaHVA}}$: *0.66; $\tau_{\text{h}*,\text{CaHVA}}$: *0.72	$c_{\text{thresh}} = 1.117$	
CACNA1D Zhang et al., 2011, Pérez-Alvarez et al., 2011	$V_{\text{offm}*,\text{CaHVA}}$: +6.6 mV; $V_{\text{slom}*,\text{CaHVA}}$: *0.75; $\tau_{\text{h}*,\text{CaHVA}}$: *0.5	$c_{\text{thresh}} = 0.282$	
	$V_{\text{offm}*,\text{CaHVA}}$: +6.6 mV; $V_{\text{slom}*,\text{CaHVA}}$: *1.19; $\tau_{\text{h}*,\text{CaHVA}}$: *0.5	$c_{\text{thresh}} = 0.178$	
	$V_{\text{offm}*,\text{CaHVA}}$: +6.6 mV; $V_{\text{slom}*,\text{CaHVA}}$: *0.75; $\tau_{\text{h}*,\text{CaHVA}}$: *1.12	$c_{\text{thresh}} = 0.302$	
	$V_{\text{offm}*,\text{CaHVA}}$: +6.6 mV; $V_{\text{slom}*,\text{CaHVA}}$: *1.19; $\tau_{\text{h}*,\text{CaHVA}}$: *1.12	$c_{\text{thresh}} = 0.188$	
CACNA1D Pinggera et al., 2015	$V_{\text{offm}*,\text{CaHVA}}$: -9.8 mV; $V_{\text{slom}*,\text{CaHVA}}$: *0.8; $V_{\text{offh}*,\text{CaHVA}}$: -15.4 mV; $V_{\text{sloh}*,\text{CaHVA}}$: *1.05	$c_{\text{thresh}} = 0.232$	
CACNA1D Azizan et al., 2013	$V_{\text{offm}*,\text{CaHVA}}$: -24.2 mV; $V_{\text{slom}*,\text{CaHVA}}$: *0.7; $V_{\text{offh}*,\text{CaHVA}}$: -14.5 mV; $V_{\text{sloh}*,\text{CaHVA}}$: *0.72; $\tau_{\text{h}*,\text{CaHVA}}$: *3.52	$c_{\text{thresh}} = 0.064$	
	$V_{\text{offm}*,\text{CaHVA}}$: +6.1 mV; $V_{\text{slom}*,\text{CaHVA}}$: *0.7; $V_{\text{offh}*,\text{CaHVA}}$: -14.5 mV; $V_{\text{sloh}*,\text{CaHVA}}$: *0.72; $\tau_{\text{h}*,\text{CaHVA}}$: *3.52	$c_{\text{thresh}} = 0.441$	
	$V_{\text{offm}*,\text{CaHVA}}$: -24.2 mV; $V_{\text{slom}*,\text{CaHVA}}$: *1.24; $V_{\text{offh}*,\text{CaHVA}}$: -14.5 mV; $V_{\text{sloh}*,\text{CaHVA}}$: *0.72; $\tau_{\text{h}*,\text{CaHVA}}$: *3.52	$c_{\text{thresh}} = 0.075$	
	$V_{\text{offm}*,\text{CaHVA}}$: +6.1 mV; $V_{\text{slom}*,\text{CaHVA}}$: *1.24; $V_{\text{offh}*,\text{CaHVA}}$: -14.5 mV; $V_{\text{sloh}*,\text{CaHVA}}$: *0.72; $\tau_{\text{h}*,\text{CaHVA}}$: *3.52	$c_{\text{thresh}} = 0.218$	
	$V_{\text{offm}*,\text{CaHVA}}$: -24.2 mV; $V_{\text{slom}*,\text{CaHVA}}$: *0.7; $V_{\text{offh}*,\text{CaHVA}}$: -14.5 mV; $V_{\text{sloh}*,\text{CaHVA}}$: *1.28; $\tau_{\text{h}*,\text{CaHVA}}$: *3.52	$c_{\text{thresh}} = 0.084$	
	$V_{\text{offm}*,\text{CaHVA}}$: +6.1 mV; $V_{\text{slom}*,\text{CaHVA}}$: *0.7; $V_{\text{offh}*,\text{CaHVA}}$: -14.5 mV; $V_{\text{sloh}*,\text{CaHVA}}$: *1.28; $\tau_{\text{h}*,\text{CaHVA}}$: *3.52	$c_{\text{thresh}} = 0.146$	
	$V_{\text{offm}*,\text{CaHVA}}$: -24.2 mV; $V_{\text{slom}*,\text{CaHVA}}$: *1.24; $V_{\text{offh}*,\text{CaHVA}}$: -14.5 mV; $V_{\text{sloh}*,\text{CaHVA}}$: *1.28; $\tau_{\text{h}*,\text{CaHVA}}$: *3.52	$c_{\text{thresh}} = 0.107$	
	$V_{\text{offm}*,\text{CaHVA}}$: +6.1 mV; $V_{\text{slom}*,\text{CaHVA}}$: *1.24; $V_{\text{offh}*,\text{CaHVA}}$: -14.5 mV; $V_{\text{sloh}*,\text{CaHVA}}$: *1.28; $\tau_{\text{h}*,\text{CaHVA}}$: *3.52	$c_{\text{thresh}} = 0.106$	*
CACNA1D Lieb et al., 2012	$V_{\text{offm}*,\text{CaHVA}}$: -17.8 mV; $V_{\text{slom}*,\text{CaHVA}}$: *0.81; $\tau_{\text{h}*,\text{CaHVA}}$: *0.77	$c_{\text{thresh}} = 0.092$	
	$V_{\text{offm}*,\text{CaHVA}}$: -17.8 mV; $V_{\text{slom}*,\text{CaHVA}}$: *0.81; $\tau_{\text{h}*,\text{CaHVA}}$: *1.31	$c_{\text{thresh}} = 0.091$	

Table S3 continued.

Gene	Parameter changes	Scaling parameter
CACNB2 Cordeiro et al., 2009	$V_{\text{offh}*,\text{CaHVA}}$: -5.2 mV; $V_{\text{sloh}*,\text{CaHVA}}$: *0.69	$c_{\text{thresh}} = 0.614$
CACNB2 Massa et al., 1995	$\tau_{\text{h}*,\text{CaHVA}}$: *1.7	$c_{\text{thresh}} = 2.000$
CACNB2 Link et al., 2009	$V_{\text{offm}*,\text{CaHVA}}$: -4.9 mV; $V_{\text{offh}*,\text{CaHVA}}$: -5.1 mV; $\tau_{\text{m}*,\text{CaHVA}}$: *0.6; $\tau_{\text{h}*,\text{CaHVA}}$: *0.6	$c_{\text{thresh}} = 0.322$
	$V_{\text{offm}*,\text{CaHVA}}$: +4.9 mV; $V_{\text{offh}*,\text{CaHVA}}$: -5.1 mV; $\tau_{\text{m}*,\text{CaHVA}}$: *0.6; $\tau_{\text{h}*,\text{CaHVA}}$: *0.6	$c_{\text{thresh}} = 0.411$
	$V_{\text{offm}*,\text{CaHVA}}$: -4.9 mV; $V_{\text{offh}*,\text{CaHVA}}$: +5.1 mV; $\tau_{\text{m}*,\text{CaHVA}}$: *0.6; $\tau_{\text{h}*,\text{CaHVA}}$: *0.6	$c_{\text{thresh}} = 0.212$
	$V_{\text{offm}*,\text{CaHVA}}$: +4.9 mV; $V_{\text{offh}*,\text{CaHVA}}$: +5.1 mV; $\tau_{\text{m}*,\text{CaHVA}}$: *0.6; $\tau_{\text{h}*,\text{CaHVA}}$: *0.6	$c_{\text{thresh}} = 1.101$
	$V_{\text{offm}*,\text{CaHVA}}$: -4.9 mV; $V_{\text{offh}*,\text{CaHVA}}$: -5.1 mV; $\tau_{\text{m}*,\text{CaHVA}}$: *1.68; $\tau_{\text{h}*,\text{CaHVA}}$: *0.6	$c_{\text{thresh}} = 0.814$
	$V_{\text{offm}*,\text{CaHVA}}$: +4.9 mV; $V_{\text{offh}*,\text{CaHVA}}$: -5.1 mV; $\tau_{\text{m}*,\text{CaHVA}}$: *1.68; $\tau_{\text{h}*,\text{CaHVA}}$: *0.6	$c_{\text{thresh}} = 0.146$
	$V_{\text{offm}*,\text{CaHVA}}$: -4.9 mV; $V_{\text{offh}*,\text{CaHVA}}$: +5.1 mV; $\tau_{\text{m}*,\text{CaHVA}}$: *1.68; $\tau_{\text{h}*,\text{CaHVA}}$: *0.6	$c_{\text{thresh}} = 0.517$
	$V_{\text{offm}*,\text{CaHVA}}$: +4.9 mV; $V_{\text{offh}*,\text{CaHVA}}$: +5.1 mV; $\tau_{\text{m}*,\text{CaHVA}}$: *1.68; $\tau_{\text{h}*,\text{CaHVA}}$: *0.6	$c_{\text{thresh}} = 0.204$
	$V_{\text{offm}*,\text{CaHVA}}$: -4.9 mV; $V_{\text{offh}*,\text{CaHVA}}$: -5.1 mV; $\tau_{\text{m}*,\text{CaHVA}}$: *0.6; $\tau_{\text{h}*,\text{CaHVA}}$: *1.66	$c_{\text{thresh}} = 0.285$
	$V_{\text{offm}*,\text{CaHVA}}$: +4.9 mV; $V_{\text{offh}*,\text{CaHVA}}$: -5.1 mV; $\tau_{\text{m}*,\text{CaHVA}}$: *0.6; $\tau_{\text{h}*,\text{CaHVA}}$: *1.66	$c_{\text{thresh}} = 0.511$
	$V_{\text{offm}*,\text{CaHVA}}$: -4.9 mV; $V_{\text{offh}*,\text{CaHVA}}$: +5.1 mV; $\tau_{\text{m}*,\text{CaHVA}}$: *0.6; $\tau_{\text{h}*,\text{CaHVA}}$: *1.66	$c_{\text{thresh}} = 0.197$
	$V_{\text{offm}*,\text{CaHVA}}$: +4.9 mV; $V_{\text{offh}*,\text{CaHVA}}$: +5.1 mV; $\tau_{\text{m}*,\text{CaHVA}}$: *0.6; $\tau_{\text{h}*,\text{CaHVA}}$: *1.66	$c_{\text{thresh}} = 1.687$
	$V_{\text{offm}*,\text{CaHVA}}$: -4.9 mV; $V_{\text{offh}*,\text{CaHVA}}$: -5.1 mV; $\tau_{\text{m}*,\text{CaHVA}}$: *1.68; $\tau_{\text{h}*,\text{CaHVA}}$: *1.66	$c_{\text{thresh}} = 0.707$
	$V_{\text{offm}*,\text{CaHVA}}$: +4.9 mV; $V_{\text{offh}*,\text{CaHVA}}$: -5.1 mV; $\tau_{\text{m}*,\text{CaHVA}}$: *1.68; $\tau_{\text{h}*,\text{CaHVA}}$: *1.66	$c_{\text{thresh}} = 0.156$
	$V_{\text{offm}*,\text{CaHVA}}$: -4.9 mV; $V_{\text{offh}*,\text{CaHVA}}$: +5.1 mV; $\tau_{\text{m}*,\text{CaHVA}}$: *1.68; $\tau_{\text{h}*,\text{CaHVA}}$: *1.66	$c_{\text{thresh}} = 0.460$
	$V_{\text{offm}*,\text{CaHVA}}$: +4.9 mV; $V_{\text{offh}*,\text{CaHVA}}$: +5.1 mV; $\tau_{\text{m}*,\text{CaHVA}}$: *1.68; $\tau_{\text{h}*,\text{CaHVA}}$: *1.66	$c_{\text{thresh}} = 0.218$
CACNB2 Hu et al., 2010	$\tau_{\text{h}*,\text{CaHVA}}$: *1.26	$c_{\text{thresh}} = 2.000$
CACNA1I Murbartián et al., 2004	$V_{\text{offma,CaLVA}}$: +1.3 mV; $V_{\text{offha,CaLVA}}$: +1.6 mV; $\tau_{\text{m}*,\text{CaLVA}}$: *0.87; $\tau_{\text{h}*,\text{CaLVA}}$: *0.8	$c_{\text{thresh}} = 2.000$
	$V_{\text{offma,CaLVA}}$: +1.3 mV; $V_{\text{offha,CaLVA}}$: +1.6 mV; $\tau_{\text{m}*,\text{CaLVA}}$: *1.45; $\tau_{\text{h}*,\text{CaLVA}}$: *0.8	$c_{\text{thresh}} = 2.000$
CACNA1I Gomora et al., 2002	$V_{\text{offma,CaLVA}}$: -4.3 mV; $V_{\text{sloma,CaLVA}}$: *1.14; $V_{\text{offha,CaLVA}}$: -4.4 mV; $V_{\text{sloha,CaLVA}}$: *0.89; $\tau_{\text{m}*,\text{CaLVA}}$: *0.53; $\tau_{\text{h}*,\text{CaLVA}}$: *0.46	$c_{\text{thresh}} = 0.968$
	$V_{\text{offma,CaLVA}}$: -4.3 mV; $V_{\text{sloma,CaLVA}}$: *1.14; $V_{\text{offha,CaLVA}}$: -4.4 mV; $V_{\text{sloha,CaLVA}}$: *1.04; $\tau_{\text{m}*,\text{CaLVA}}$: *0.53; $\tau_{\text{h}*,\text{CaLVA}}$: *0.46	$c_{\text{thresh}} = 2.000$
ATP2A2 Ji et al., 2000	$\gamma_{[\text{Ca}^{2+}]}$: *0.6	$c_{\text{thresh}} = 0.224$
ATP2B2 Fakira et al., 2012	$\tau_{[\text{Ca}^{2+}]}$: *1.97	$c_{\text{thresh}} = 0.231$
ATP2B2 Empson et al., 2010	$\tau_{[\text{Ca}^{2+}]}$: *1.5; $c_{\text{min},[\text{Ca}^{2+}]}$: *1.4	$c_{\text{thresh}} = 0.218$
ATP2B2 Ficarella et al., 2007	$\tau_{[\text{Ca}^{2+}]}$: *4.45	$c_{\text{thresh}} = 0.105$
ATP2B2 Giacomello et al., 2011	$c_{\text{min},[\text{Ca}^{2+}]}$: *1.1	$c_{\text{thresh}} = 1.625$
SCN1A Cestèle et al., 2008	$V_{\text{offm,Nat}}$: -0.3 mV; $V_{\text{offh,Nat}}$: +5 mV; $V_{\text{slom,Nat}}$: *1.15; $V_{\text{sloh,Nat}}$: *1.23	$c_{\text{thresh}} = 0.049$
SCN1A Vanmolkot et al., 2007	$V_{\text{offm,Nat}}$: +2.8 mV; $V_{\text{offh,Nat}}$: +9.6 mV; $V_{\text{slom,Nat}}$: *0.984; $V_{\text{sloh,Nat}}$: *1.042	$c_{\text{thresh}} = 0.063$
SCN1A Volkers et al., 2011	$V_{\text{offm,Nat}}$: -4.0 mV; $V_{\text{offh,Nat}}$: -5.8 mV; $V_{\text{slom,Nat}}$: *0.92; $V_{\text{sloh,Nat}}$: *1.13; $\tau_{\text{h}*,\text{Nat}}$: *1.47	$c_{\text{thresh}} = 0.273$
SCN1A Volkers et al., 2011	$V_{\text{offm,Nat}}$: -8.1 mV; $V_{\text{offh,Nat}}$: +2.2 mV; $V_{\text{slom,Nat}}$: *0.97; $V_{\text{sloh,Nat}}$: *0.97; $\tau_{\text{h}*,\text{Nat}}$: *1.59	$c_{\text{thresh}} = 0.037$
SCN1A Cestèle et al., 2013	$V_{\text{offm,Nat}}$: +6.0 mV; $V_{\text{slom,Nat}}$: *1.16; $\tau_{\text{h}*,\text{Nat}}$: *1.29	$c_{\text{thresh}} = 0.129$
SCN1A Mantegazza et al., 2005	$V_{\text{offm,Nat}}$: +10.0 mV; $V_{\text{offh,Nat}}$: -0.6 mV; $V_{\text{slom,Nat}}$: *1.15; $V_{\text{sloh,Nat}}$: *1.14	$c_{\text{thresh}} = 0.062$
HCN1 Ishii et al., 2007	$V_{\text{offm}*,\text{h}}$: -26.5 mV; $V_{\text{slom}*,\text{h}}$: *0.64	$c_{\text{thresh}} = 0.296$
HCN1 Lesso and Li, 2003	$V_{\text{offm}*,\text{h}}$: -25.9 mV; $V_{\text{slom}*,\text{h}}$: *0.6	$c_{\text{thresh}} = 0.282$
	$V_{\text{offm}*,\text{h}}$: +17.7 mV; $V_{\text{slom}*,\text{h}}$: *0.6	$c_{\text{thresh}} = 0.807$
HCN1 Wemhöner et al., 2015	$V_{\text{offm}*,\text{h}}$: +3.9 mV; $\tau_{\text{m}*,\text{h}}$: *0.88	$c_{\text{thresh}} = 1.226$
KCNB1 Bocksteins et al., 2011	$V_{\text{offm,Kp}}$: +5 mV; $V_{\text{offh,Kp}}$: +3 mV; $V_{\text{slom,Kp}}$: *1.11; $V_{\text{sloh,Kp}}$: *0.86; $\tau_{\text{m}*,\text{Kp}}$: *0.5; $\tau_{\text{h}*,\text{Kp}}$ *0.53	$c_{\text{thresh}} = 2.000$
KCNB1 Bocksteins et al., 2011	$V_{\text{offm,Kp}}$: +1 mV; $V_{\text{offh,Kp}}$: -6 mV; $V_{\text{slom,Kp}}$: *1.22; $V_{\text{sloh,Kp}}$: *1.0; $\tau_{\text{m}*,\text{Kp}}$: *0.89; $\tau_{\text{h}*,\text{Kp}}$ *1.13	$c_{\text{thresh}} = 2.000$
KCNB1 Bocksteins et al., 2011	$V_{\text{offm,Kp}}$: +6 mV; $V_{\text{offh,Kp}}$: -8 mV; $V_{\text{slom,Kp}}$: *1.33; $V_{\text{sloh,Kp}}$: *1.0; $\tau_{\text{m}*,\text{Kp}}$: *0.5; $\tau_{\text{h}*,\text{Kp}}$: *0.87	$c_{\text{thresh}} = 2.000$
KCNB1 Bocksteins et al., 2011	$V_{\text{offm,Kp}}$: -28 mV; $V_{\text{offh,Kp}}$: -27 mV; $V_{\text{slom,Kp}}$: *1.11; $V_{\text{sloh,Kp}}$: *0.71; $\tau_{\text{m}*,\text{Kp}}$: *1.13; $\tau_{\text{h}*,\text{Kp}}$: *2.27	$c_{\text{thresh}} = 2.000$
KCNB1 Bocksteins et al., 2011	$V_{\text{offm,Kp}}$: +14 mV; $V_{\text{offh,Kp}}$: -21 mV; $V_{\text{slom,Kp}}$: *2.0; $V_{\text{sloh,Kp}}$: *1.0; $\tau_{\text{m}*,\text{Kp}}$: *0.39; $\tau_{\text{h}*,\text{Kp}}$ *1.2	$c_{\text{thresh}} = 2.000$
KCNB1 Bocksteins et al., 2011	$V_{\text{offm,Kp}}$: -13 mV; $V_{\text{offh,Kp}}$: -13 mV; $V_{\text{slom,Kp}}$: *1.33; $V_{\text{sloh,Kp}}$: *0.71; $\tau_{\text{m}*,\text{Kp}}$: *0.95; $\tau_{\text{h}*,\text{Kp}}$: *5.13	$c_{\text{thresh}} = 2.000$

For those unscaled variants that did not violate the conditions 1–5, we sought for the threshold effect up to twice the original effect, i.e., $c < 2$. If the model variant still obeyed the conditions, we considered the original model variant as the $\epsilon = \frac{1}{2}$ variant and applied other scalings with respect to this choice.

The model parameters affected by the variants include quantities of various roles and dimensions (mV, mM, ms, etc.), which calls for a careful consideration of how to scale them properly. We chose to perform this so that those parameters that may receive both negative and positive values were scaled linearly, while the parameters that receive only positive values were scaled on the logarithmic scale. More specifically, this means that the differences in offset and reverse potentials ($V_{\mathrm{offm}*}$, $V_{\mathrm{offh}*}$, E_{Ih}) between control and the model variant were expressed as an additive term ($\pm x$ mV), so this term x was multiplied by a parameter $c \in [0, 1]$ in the downscaling procedure. By contrast, the differences in all the other model parameters ($V_{\mathrm{offc}*}$, $V_{\mathrm{slo}*}$, τ_*, c_*, γ_*) between control and the variant were expressed as a multiplication ($\times x$), so the downscaling caused this factor x to be exponentiated by the same parameter c. This procedure permits a continuum of parameter changes in the range $c \in [0, 1]$ that is directly applicable to amplified ($c > 1$) parameter changes as well.

S1.3 Oscillatory Poisson process

In this work, we used both stationary (e.g. in Figure 1) and non-stationary (e.g. in Figure 2) Poisson processes for the activation times of the background synapses. A stationary Poisson process is characterized by an exponential inter-event interval distribution

$$f(t) = \begin{cases} \lambda \exp(-\lambda t), \text{ if } t \geq 0 \\ 0, \text{ otherwise} \end{cases},$$

where λ is a constant, and the resulting inter-event intervals are independent of each other. An extension of this process is a non-stationary (or non-homogeneous) Poisson process, where the rate term λ is a function of time (Tran-Gia, 1983). We formulate the rate term of the inter-event interval distribution as

$$\lambda(t) = (1 + 0.25 \sin(2\pi f t))\lambda_0,$$

where λ_0 is a constant average rate term (the same values used as in Hay and Segev, 2015, namely, 0.72 Hz for excitatory inputs and 7.0 Hz for inhibitory inputs), and f is the frequency of the input oscillations (in our work, this term ranged from 0.5 Hz to 15 Hz). In this work, we calculated an empirical distribution for the timings of the background synaptic inputs for 30 equally spaced phases of the oscillation, and in the beginning of each network simulation, we picked the timings by sampling from this distribution. This was done iteratively, starting at $t = 0$, so that the phase (in the oscillation of frequency f) at which the previous background synaptic input arrived determined which of the 30 distributions would be used for picking the next inter-event interval. Figure S2A–B shows six empirical inter-event interval distributions for different phases of a 0.75-Hz oscillation and their cumulative distributions. These cumulative distributions were used for sampling the inter-event intervals for glutamatergic background synapses. Figure S2C shows the resulting background synaptic spike times for a range of frequencies.

S1.4 Spectral analysis

We determined the prevalence of different frequency components in the population spike train data produced by the model using standard spectral analysis. Given a population spike train $s(t) = \sum_{j=1}^{N_{\mathrm{spikes}}} \delta_{t_j}(t)$, where the variables t_j represent the spike times of all neurons and functions δ_{t_j} are Dirac the delta functions, the spectral power was determined as

$$P_s(f) = |F_s(f)|^2, \tag{S2}$$

where $F_s(f)$ is the Fourier component for the frequency f. This component was determined as

$$F_s(f) = \int_{-\infty}^{\infty} s(t) e^{-2\pi i t f} dt = \sum_{j=1}^{N_{\mathrm{spikes}}} e^{-2\pi i t_j f}, \tag{S3}$$

where i is the imaginary unit.

The power spectra of the EEG signal were determined as follows. First, the EEG signal was smoothened using a bin size of $\Delta t = 5$ ms, giving us a signal

$$s(t) = \sum_{k=0}^{N_s - 1} s_k \chi_{[k\Delta t, (k+1)\Delta t)}(t).$$

Here, $N_s = \lfloor \frac{T}{\Delta t} \rfloor$ is the number of bins, where T denotes the length of the simulation, and the bins span half-open intervals $[k\Delta t, (k+1)\Delta t)$, each of length Δt. The indicator functions χ define the temporal bases of the bins as follows:

$$\chi_S(t) = \begin{cases} 1, \text{ if } t \in S \\ 0, \text{ otherwise} \end{cases}.$$

The Fourier component for the frequency f of the signal s was determined as

$$F_s(f) = \int_{-\infty}^{\infty} s(t)e^{-2\pi itf}dt = \sum_{k=0}^{N_s-1} s_k \int_{k\Delta t}^{(k+1)\Delta t} e^{-2\pi itf}dt = \sum_{k=0}^{N_s-1} \frac{s_k}{-2\pi if}e^{-2\pi ifk\Delta t}(e^{-2\pi if\Delta t} - 1), \tag{S4}$$

when $f \neq 0$. For $f = 0$,

$$F_s(f) = \Delta t \sum_{k=0}^{N_s-1} s_k. \tag{S5}$$

The spectral power of the EEG signal was then determined by Equation S2.

S1.5 Prediction of EEG potentials

In a subset of our results, we calculated the EEG signature of our L5PC network using a simplified model of the human head comprising four concentric spheres (the so-called "four-sphere head model") (Srinivasan et al., 1998; Næss et al., 2017). In this model, the brain (radius 7.9 cm) is first surrounded by a 0.1-cm layer of cerebrospinal fluid (CSF), then a 0.5-cm layer of skull, and finally a 0.5-cm layer of scalp on top of which the recording electrode lies. The conductivity is assumed to be constant within each layer (brain: 0.3 S/m; CSF: 1.5 S/m; skull: 0.015 S/m; scalp: 0.3 S/m). The conductivity outside the scalp layer was 0 S/m. We placed the somata of our neuron population on a tangential plane at a distance 1.5 mm from the surface of the brain so that the surface-areal density of our neurons was approximately $0.1/\mu m^2$, as suggested by reports from staining experiments (Meyer et al., 2010; Chen et al., 2014). To do this, the first soma was placed at the origin of the plane. Then, the next 6 neuron somata were equidistantly placed on the perimeter of an origin-centered circle with radius 56 μm — the number of somata (6) was picked as the maximal number with which the distance between two somata on the perimeter did not exceed 56 μm. This procedure was repeated using circles with radii 2×56 μm, 3×56 μm, etc., until all 150 somata were placed. The apical dendrites of the L5PCs projected from the somata in the direction orthogonal to the tangential plane, while the basal dendrites were assumed to project to the opposite direction — approximately toward the center of the head. The recording electrode was located 10 μm inside the outer radius of the scalp. We first calculated the dipole moment of our L5PC network based on the trans-membrane currents of each membrane compartment of our neuron population. Due to the alignment of our L5PCs, the radial components of the dipole moments were large while the tangential components were negligible. We then applied the analytical formula estimating the EEG scalp surface potential of this population at the recording electrode (see Næss et al., 2017 for details). The inhibitory population, when present, did not affect the EEG signature as it consisted of point neurons (data not shown).

S2 Supplementary Figures

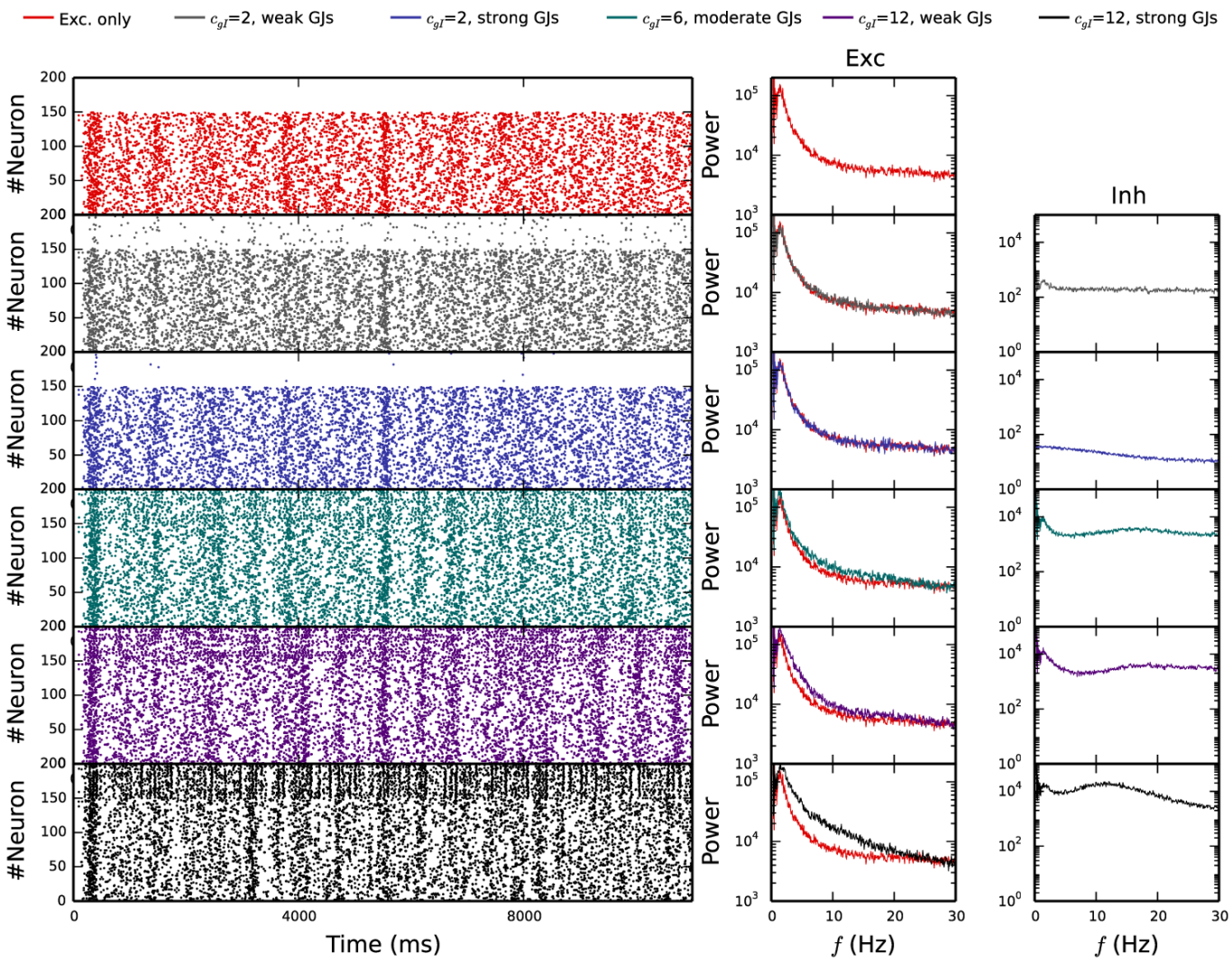

Figure S1: Interactions between excitatory and inhibitory populations in networks with different strengths of synapses converging to the inhibitory neurons. The left-hand column shows the population spike trains of the L5PC-only network and those of five excitatory-inhibitory networks with different values of c_{gI} and g_{GJ} (and of c_{gEE}, which is determined separately for each combination of c_{gI} and g_{GJ}). The neuron indices (y-axis) 0-149 show the data from the 150 L5PCs and indices 150-199 show the data from the 50 basket cells. The middle column shows the power spectrum of the L5PC population spike train, averaged across N_{samp}=100 repetitions. In the excitatory-inhibitory networks, the power spectrum is overlaid with the power spectrum of the L5PC-only network for comparison. The right-hand column shows the power spectrum of the basket cell population spike train, averaged across N_{samp}=100 repetitions.

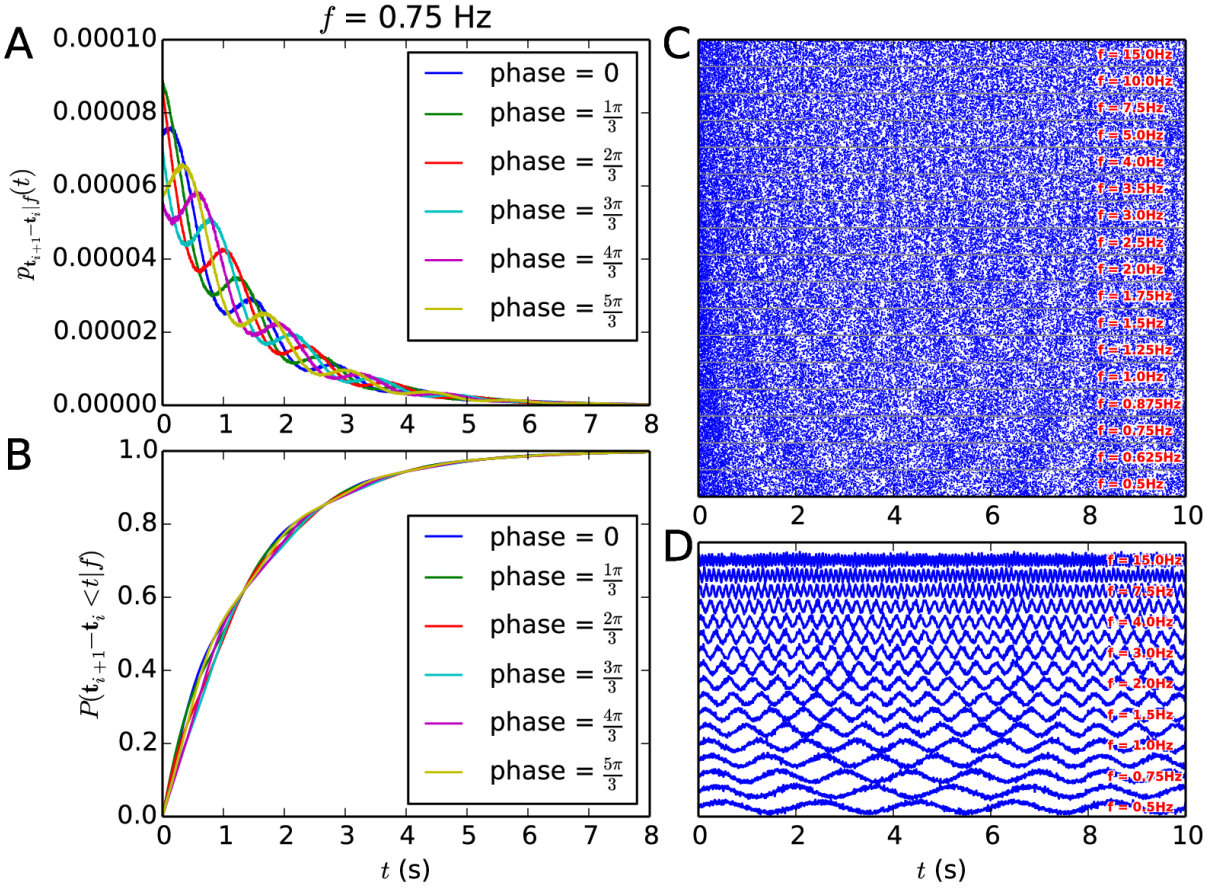

Figure S2: **Illustration on oscillatory Poissonian statistics.** **A**: Probability density function of the inter-event interval for an oscillatory Poisson process of 0.75 Hz at six different phases. The temporal resolution of 10 kHz was used for generating the data, but here the results are summed across 25 bins. **B**: Cumulative distribution functions of the probability density functions in (A). **C**: Background synaptic activation times that obey the oscillatory Poissonian statistics with different frequencies. **D**: Event rate profiles of the background synaptic spike trains in (C), summed across the 10000 glutamatergic synaptic processes that were independent of each other, bin size 25 ms.

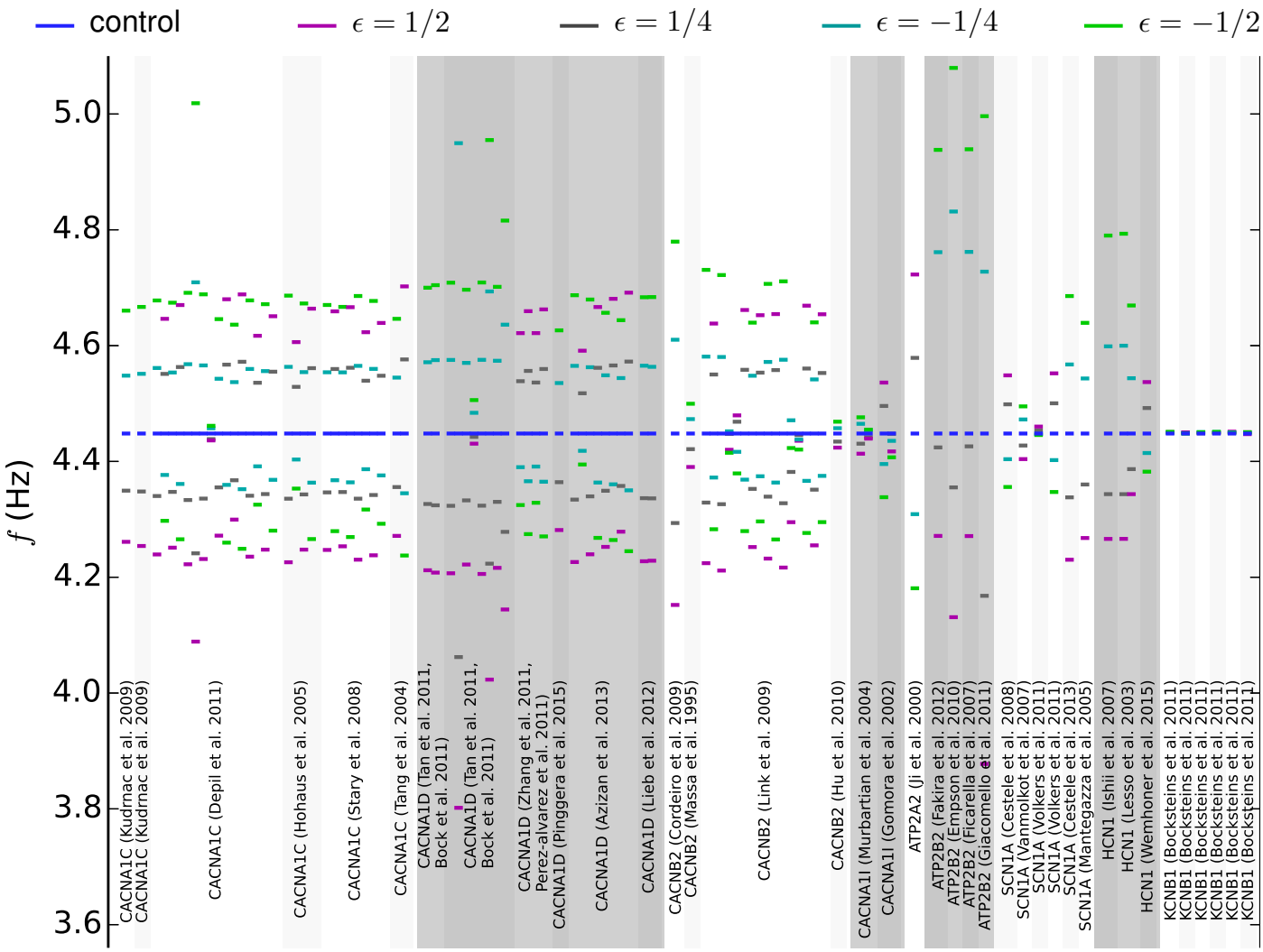

Figure S3: **Model variants affect the average gain of the L5PC network**. The y axis shows the average of the gain curve values in Figure 1 for each model variant of Table S3. Blue: control network (no variants), other colors: downscaled variants with different scaling parameter ϵ. For clarity, the model variants of the same gene are highlighted with the same grayscale background (white or gray), and in each band, the divisions to different variants are represented by slight changes in the background color.

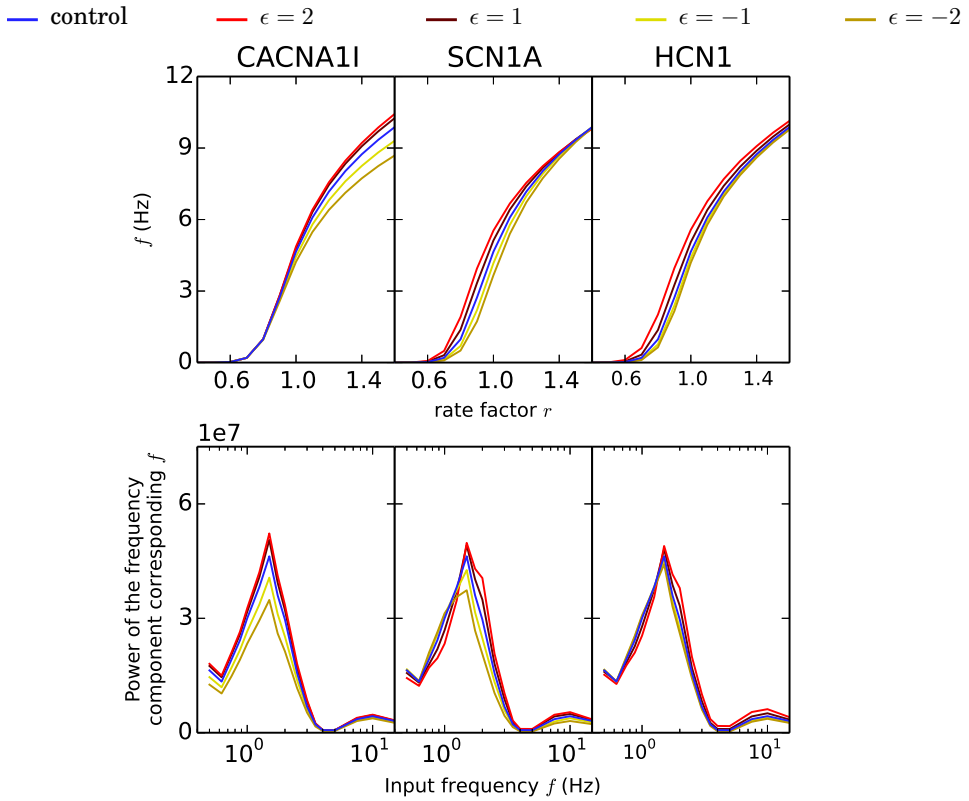

Figure S4: **Effects of stronger model variants of *CACNA1I*, *SCN1A*, and *HCN1***. The unscaled versions of these model variants are the same as those of Figures 1 and 2, but the scaling parameters are four-fold ($\epsilon = 1$ and $\epsilon = 2$). The upper panels correspond to the simulations of Figure 1, and the lower panels correspond to those of Figure 2. Blue: control network (no variants), other colors: downscaled variants with different scaling parameter ϵ. The *CACNA1I* model variants show typical increases or decreases in network gain, which are in line with the effects on the response to oscillations across frequencies. By contrast, the *SCN1A* and *HCN1* model variants show larger amplification/deamplification of network firing rates at low levels of input, and have varied effects on the oscillation response curves.

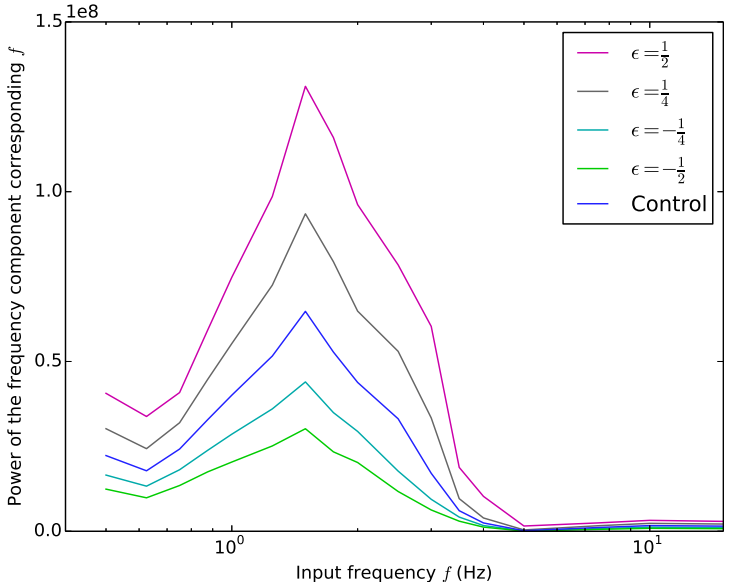

Figure S5: **Effects of the combination of model variants of Figures 1 and 2 on response to oscillations predicted by the network model consisting of L5PCs with reconstructed morphology**. The network model is the same as that in Hay and Segev, 2015, except that we used the non-stationary, oscillatory Poisson process for the background synapse activation times (see Methods). The networks are simulated for $T = 10$ s without any of the additional external stimulations that were used in Hay and Segev, 2015. Here, we considered the background oscillation frequencies f=0.5, 0.625, 0.75, 0.875, 1.0, 1.25, 1.5, 1.75, 2.0, 2.5, 3.0, 3.5, 4.0, 5.0, 7.5, 10.0, and 15.0 Hz. For each background frequency, N_{samp}=9 networks were simulated with different random number seeds, and the power spectrum of each resulting population spike train was evaluated. The y axis shows the mean of the power component corresponding to the input frequency across these nine samples. The responses of the full-morphology L5PC network model were very similar to those of the reduced-morphology L5PC network model, illustrated in Figure 2.

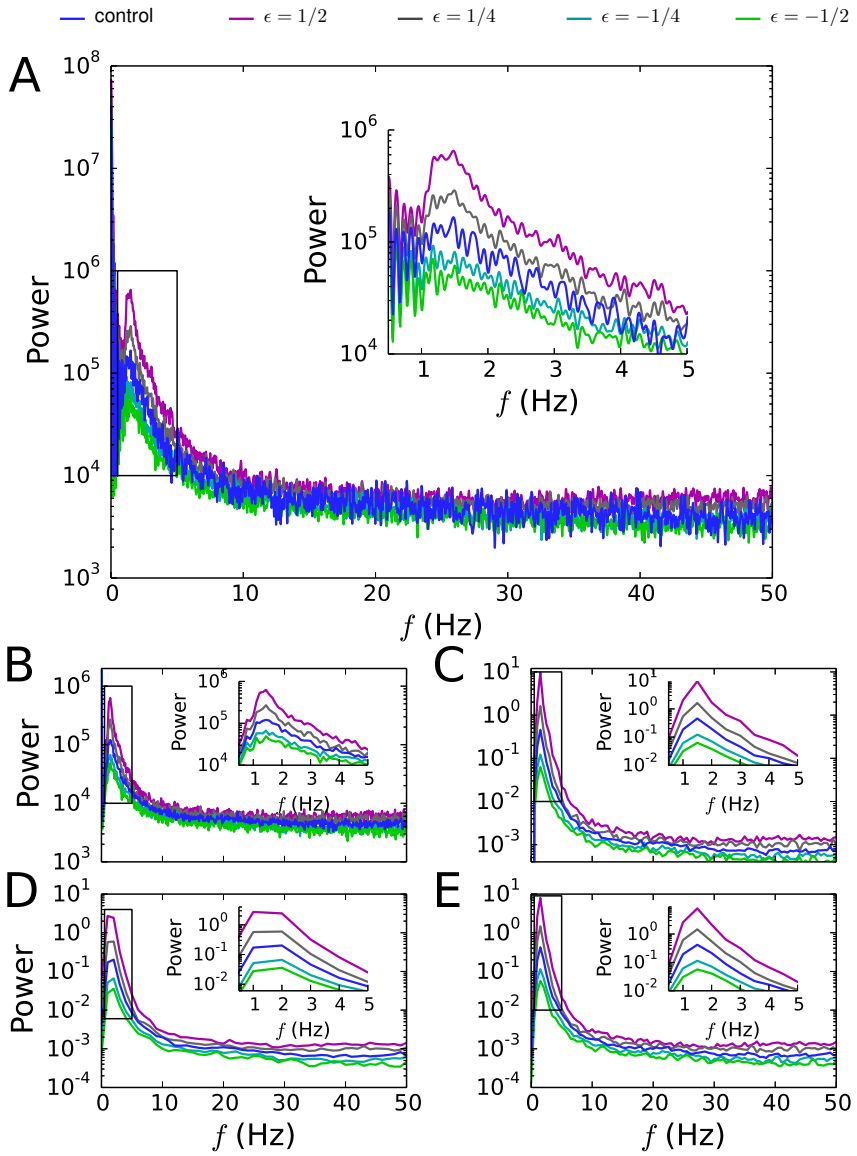

Figure S6: **Model variants affect the magnitude of the delta-frequency oscillations originating in the L5PC network**. Simulation of networks of 150 L5PCs, where the background synapse activation times were stationary Poisson processes (i.e., no oscillation in the inputs) with activation rates $f = 0.72$ Hz (excitatory synapses) and $f = 7.0$ Hz (inhibitory synapses). The blue curve represents the control network, while other colors represent networks where each L5PC employed a combination of the model variants (see Figure 1C). The inset zooms in on the delta frequency range. The y-axis power values (arbitrary units) were averaged across N_{samp}=24–73 simulations with different random number seeds. **A**: Spectral power of the population spike train, calculated using Equations S2 and S3. The median of power component corresponding to the frequency 1.5 Hz was significantly different between the $\epsilon = \frac{1}{2}$ variant and control networks (U-test, p<0.01, 72 vs. 24 samples). **B**–**E**: Spectral powers of the binned spiking frequency data using standard fast Fourier methods. The population spike trains were first discretized to firing rate vectors using a bin size of 5 ms. In (B), the fast Fourier transform was taken from the whole signal, whereas in (C)–(E), Welch's method was used. In (C), the boxcar filtering window was applied, and the window length was 2 seconds with a 1-second overlap. In (D) and (E), the Hamming filtering window was applied, and the window length was 1 second without an overlap (D) or 2 seconds with a 1-second (E) overlap. The power spectra were determined, and the values shown are averages across the N_{samp} simulations (and further across the windows in (C)–(E)).

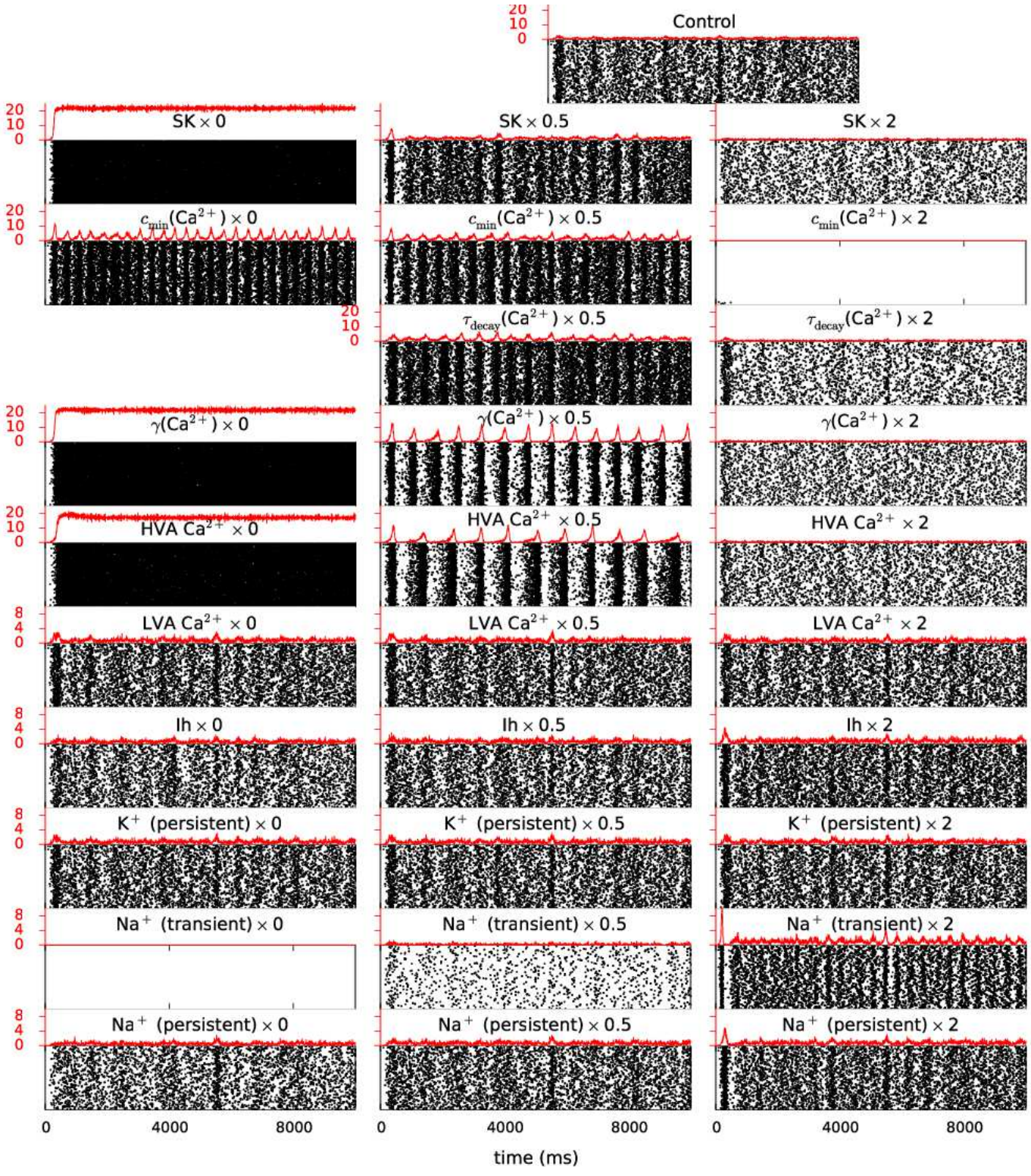
Control
SK × 0
SK × 0.5
SK × 2
$c_{min}(Ca^{2+}) \times 0$
$c_{min}(Ca^{2+}) \times 0.5$
$c_{min}(Ca^{2+}) \times 2$
$\tau_{decay}(Ca^{2+}) \times 0.5$
$\tau_{decay}(Ca^{2+}) \times 2$
$\gamma(Ca^{2+}) \times 0$
$\gamma(Ca^{2+}) \times 0.5$
$\gamma(Ca^{2+}) \times 2$
HVA Ca^{2+} × 0
HVA Ca^{2+} × 0.5
HVA Ca^{2+} × 2
LVA Ca^{2+} × 0
LVA Ca^{2+} × 0.5
LVA Ca^{2+} × 2
Ih × 0
Ih × 0.5
Ih × 2
K^+ (persistent) × 0
K^+ (persistent) × 0.5
K^+ (persistent) × 2
Na^+ (transient) × 0
Na^+ (transient) × 0.5
Na^+ (transient) × 2
Na^+ (persistent) × 0
Na^+ (persistent) × 0.5
Na^+ (persistent) × 2
0
4000
8000
time (ms)

Figure S7: **(Previous page) Parameteric analysis on the effects of maximal ion-channel conductances of different current species and parameters controlling the Ca^{2+} dynamics on the network spiking behavior.** The x axis shows the time, and the y axis shows the neuron index (black dots) and the firing rate (red curves above the spike trains, values in spikes/millisecond, binned with 5-ms resolution). The uppermost panel shows the population spike train in the control network, while the rows below show the population spike trains where one of the model parameters is set to zero (left panels), half of the original value (middle panels), or double the original value (right panels). The largest effects are caused by alterations of SK and HVA Ca^{2+} channel conductances (first and fifth row) as well as those of the parameter γ (fourth row), which describes the fraction of the Ca^{2+} ions (entering the cell with the HVA and LVA Ca^{2+} currents) that remains unbuffered in the sub-membrane space and thus ready to interact with SK channels and PMCA pumps (see Equation S1). Decreasing the value of these parameters directly or indirectly decreases the SK currents, leading to radically increased spiking. Largely similar effects are conveyed by parameters c_{min} and τ_{decay} (second and third row), which describe the resting level of intracellular $[Ca^{2+}]$ and the rate of its decay, respectively. The extreme value τ_{decay}=0 is not shown due to the singularity it causes, but the solution converges toward the case γ=0 as the Ca^{2+} transients return to zero infinitely fast. Doubling the value of c_{min} strengthened the SK currents to the extent that almost no spiking occurred at all. The parameters of the sixth to tenth row describe the maximal conductances of the rest of the Hay model channels (except for Kv3.1 and I_{m} channels) — note the finer scale of the y-axes compared to the panels in the first to fifth rows. Of these, only the transient Na^{+} channel conductance has a very large effect — completely blocking the transient Na^{+} channel inhibits the spiking behavior as expected. Notable effects are conveyed also by changes in maximal conductances of I_{h} channel and persistent Na^{+} channel. Interestingly, changes in the LVA Ca^{2+} channel conductance show very modest effects, which are best seen as a modest decrease in the peak of the firing rate curve in response to an increase in the channel conductance. However, our previous studies (Mäki-Marttunen et al., 2016; Mäki-Marttunen et al., 2017) as well as the analyses of Figures 1 and 2 show that changing the channel kinetics and voltage dependence of the LVA Ca^{2+} channel can have strong effects.

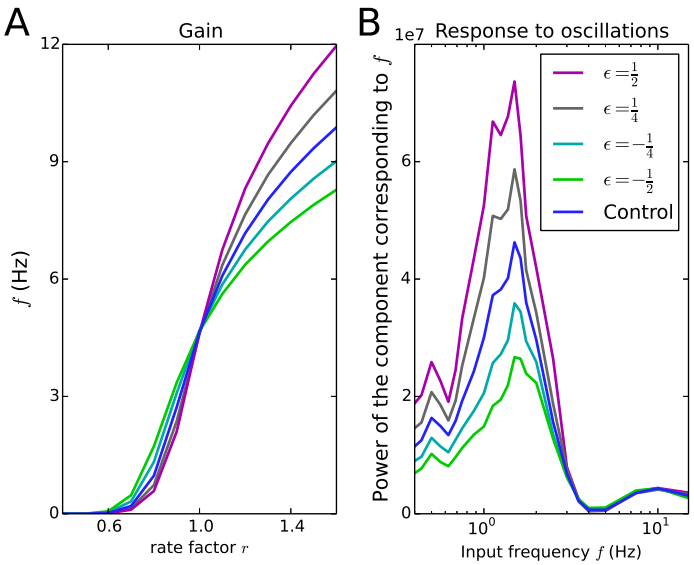

Figure S8: **A combination of model variants, when compensated by synaptic scaling, changes the response to delta-band oscillatory inputs without having a large effect on responses to inputs with higher frequencies.** The combination of the model variants is the same as in Figures 1C and 2C, but each of the scalings is compensated by a decrease or increase in numbers of background synaptic inputs as follows: $\epsilon = \frac{1}{2}$ (purple): $N_{\mathrm{synE}} = 8717$, $N_{\mathrm{synI}} = 2179$; $\epsilon = \frac{1}{4}$ (gray): $N_{\mathrm{synE}} = 9291$, $N_{\mathrm{synI}} = 2323$; $\epsilon = -\frac{1}{4}$ (cyan): $N_{\mathrm{synE}} = 10940$, $N_{\mathrm{synI}} = 2735$; $\epsilon = -\frac{1}{2}$ (green): $N_{\mathrm{synE}} = 12232$, $N_{\mathrm{synI}} = 3058$. **A**: Gain curves, see Figure 1C for details. The curves intersect at $r = 1.0$ as the numbers of background synaptic inputs were fitted for each scaling separately such that the numbers of spikes match for this value of r. **B**: Powers of the frequency components corresponding to the frequency of the oscillating background synaptic inputs, see Figure 2C for details. The data were averaged over N_{samp}=7–11 (A) or 9–11 (B) network simulations with different random number seeds.

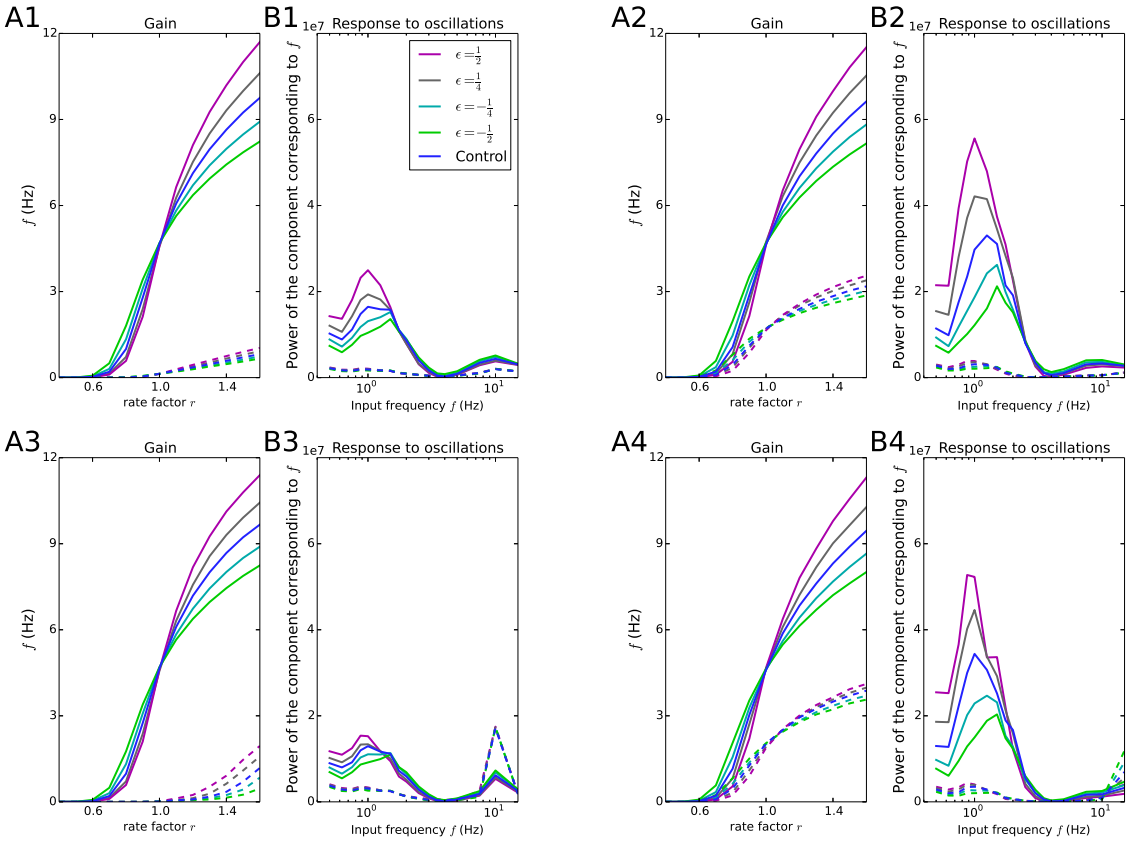

Figure S9: **Combination of model variants, when compensated by synaptic scaling, changed the response of the excitatory-inhibitory network to delta-band oscillatory inputs without a large effect on responses to higher frequencies.** The combination of the model variants was the same as in Figure S8, but here the L5PC population was coupled with an inhibitory population of size N=50 (see Section S1.1.5). The different panels show network models where the chemical synaptic conductances (c_{gI}) at the inhibitory neurons and the gap junction conductances (g_{GJ}) were different. See Section S1.1.5 for more details on the construction of this excitatory-inhibitory network model. A1, B1: Weak synaptic inputs to inhibitory population ($c_{\mathrm{gI}} = 2.0$), weak gap junctions ($g_{\mathrm{GJ}} = 0.02$ nS). A2, B2: Strong synaptic inputs to inhibitory population ($c_{\mathrm{gI}} = 12.0$), weak gap junctions ($g_{\mathrm{GJ}} = 0.02$ nS). A3, B3: Weak synaptic inputs to inhibitory population ($c_{\mathrm{gI}} = 2.0$), strong gap junctions ($g_{\mathrm{GJ}} = 2$ nS). A4, B4: Strong synaptic inputs to inhibitory population ($c_{\mathrm{gI}} = 12.0$), strong gap junctions ($g_{\mathrm{GJ}} = 2$ nS). Each of the networks was compensated by a decrease or increase in numbers of background synaptic inputs ($N_{\mathrm{synE}} = 10000\alpha$ and $N_{\mathrm{synI}} = 2500\alpha$) to make the networks produce the same firing rates for $r = 1.0$. In panels A1, B1, the alpha coefficients are the following $\epsilon = \frac{1}{2}$ (purple): $\alpha = 0.9214$; $\epsilon = \frac{1}{4}$ (gray): $\alpha = 0.9554$; $\epsilon = -\frac{1}{4}$ (cyan): $\alpha = 1.0483$; $\epsilon = -\frac{1}{2}$ (green): $\alpha = 1.1062$. In A2 and B2, the corresponding α coefficients were 0.9117, 0.959, 1.0539, and 1.1172, in A3 and B3 0.9215, 0.9554, 1.0483, 1.106, and in A4 and B4 0.9056, 0.9512, 1.0504, 1.1134. Panels A show the gain curves as in Figure S8A (averaged over N_{samp}=6–10 repetitions), and panels B show the powers of the frequency components corresponding to the frequency of the oscillating background synaptic inputs, see Figure S8B (averaged over N_{samp}=11–15 repetitions). Background oscillation frequencies f=0.5, 0.625, 0.75, 0.875, 1.0, 1.25, 1.5, 1.75, 2.0, 2.5, 3.0, 3.5, 4.0, 5.0, 7.5, 10.0, and 15.0 Hz were considered. The qualitative predicted effects of the model variants were robust across the different cases: despite the compensation by the synaptic scaling, the model variants increased the response of the network to inputs oscillating at low delta-band frequencies (especially around 1 Hz) while they mildly decreased the amplitude of the responses to inputs oscillating in higher frequencies.

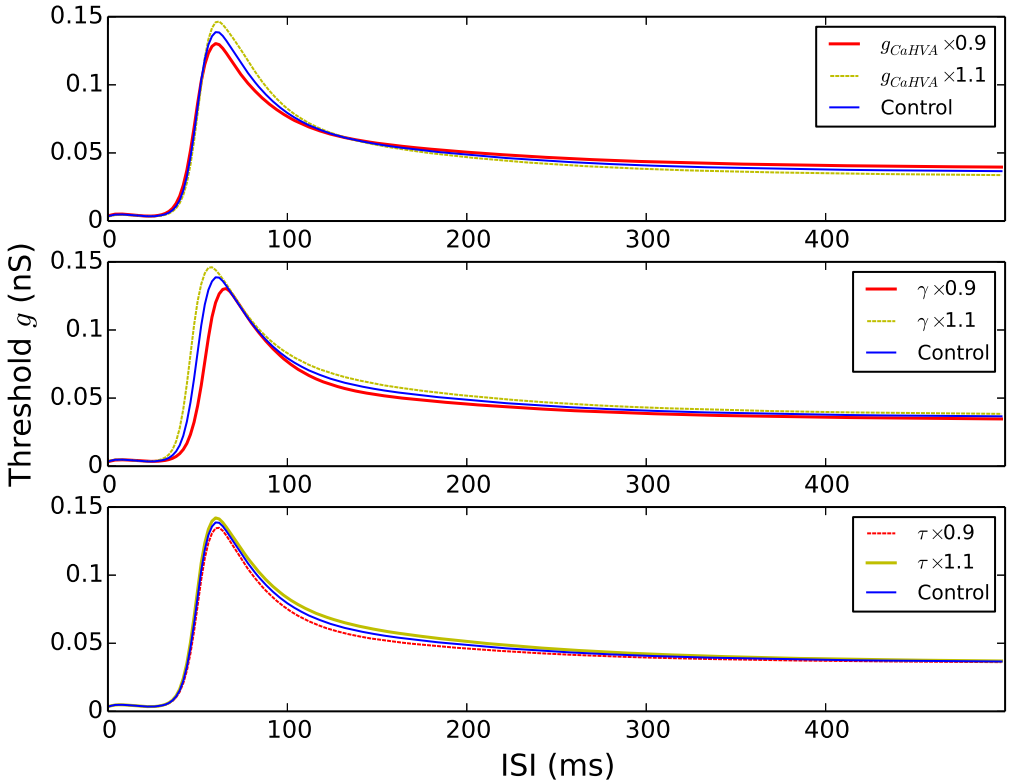

Figure S10: **Effects of single-parameter variants of Figure 4 on single-cell prepulse inhibition.** The curves show the threshold conductance for the second input arriving simultaneously to the 3000 synapses located at the apical dendrite. See Figure 5A for details. The three panels correspond to the parameter changes related to altered expression of *CACNA2D3* or *CACNB3* (top), *ATP2A2* (middle), and *ATP2B1* (bottom). In the cases of *CACNA2D3*, *CACNB3* and *ATP2A2*, the under-expression of the underlying gene caused a deficit of the single-cell prepulse inhibition at 60 ms. The under-expression of *ATP2B1*, by contrast, due to the slower decay of cytosolic Ca^{2+} implies longer-lasting SK currents and thus slightly increased single-cell prepulse inhibition at 60 ms. See Figure 4 for the corresponding effects of these model variants on L5PC network gain and response to oscillations.

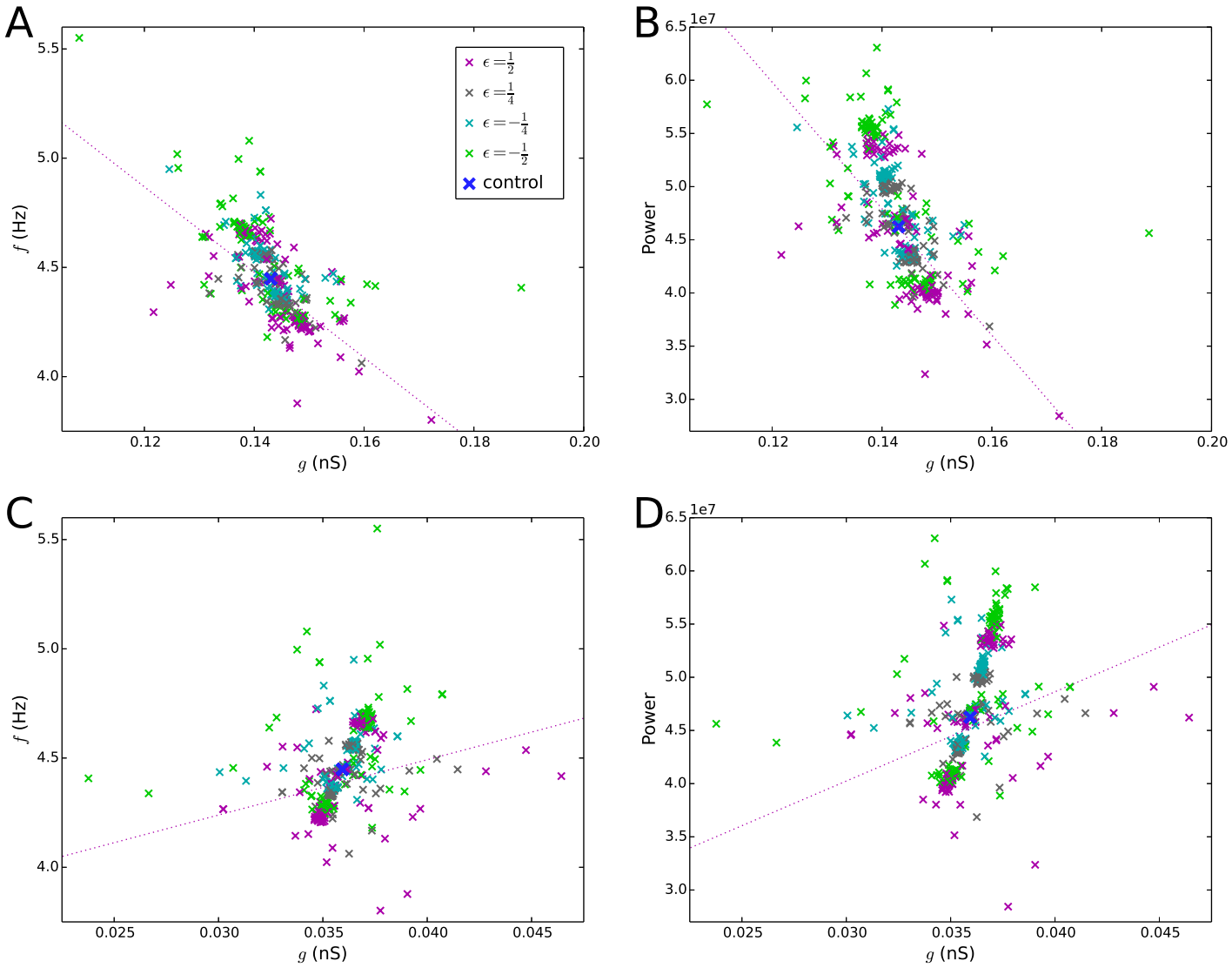

Figure S11: **The network gain and power of the response to delta-frequency oscillations are negatively correlated with the prepulse inhibition.** The y-axis data are from the single-cell simulations, and the x-axis data are from the network simulations. In each simulation, the L5PC or the L5PCs are equipped with one of the model variants of Table S3. **A**: The average network gain (see Figure S3) is plotted against the threshold conductance for the second stimulus at 60 ms (see Figure S9). **B**: The power of the network response (see Figure 2) to inputs oscillating in a 1.5-Hz frequency plotted against the threshold conductance for the second stimulus at 60 ms. **C**: The average network gain plotted against the threshold conductance for the second stimulus at 300 ms. **D**: The power of the network response to inputs oscillating in a 1.5-Hz frequency plotted against the threshold conductance for the second stimulus at 300 ms. The data show that the average network gain and the power of the network response to inputs oscillating in a 1.5-Hz frequency are anticorrelated (correlation coefficients -0.674 and -0.671) with the threshold conductance for the second apical stimulus, applied 60 ms after the first stimulus in a single L5PC. By contrast, the data show that the network gain and the network response to 1.5-Hz inputs are mildly correlated (correlation coefficients 0.296 and 0.271) with the threshold conductance for the second apical stimulus applied 300 ms after the first stimulus. The dashed lines show the best fits to the data for $\epsilon = \frac{1}{2}$ variants.

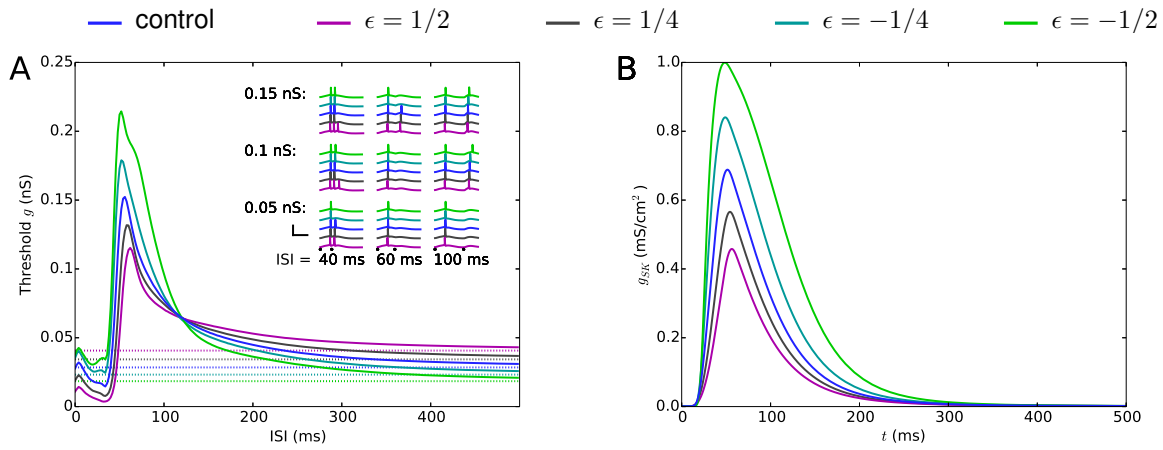

Figure S12: **The single-L5PC model predicts that the combination of gain-inducing model variants causes deficits in prepulse inhibition.** **A**: The solid curves show the threshold conductance needed for the second input to induce an additional spike, given that the prestimulus was 10% above the threshold conductance at rest (shown by the dashed lines). For the positively scaled variants ($\epsilon = \frac{1}{2}$ and $\epsilon = \frac{1}{4}$), a deficit in prepulse inhibition, i.e., lowered threshold conductance for the second input, is observed when the interval between the first and the second inputs is approximately 40–100 ms. The insets show the somatic membrane potential traces following the two stimuli, given different intervals and synaptic conductances of the second stimulus. See Figure 5 for details. **B**: The SK current, recorded at the "hot zone" of Ca^{2+} channels (720 µm from the soma at the apical dendrite) in the single-L5PC model of Hay et al., 2011, shows time course similar to the prepulse inhibition threshold shown in panel (A).

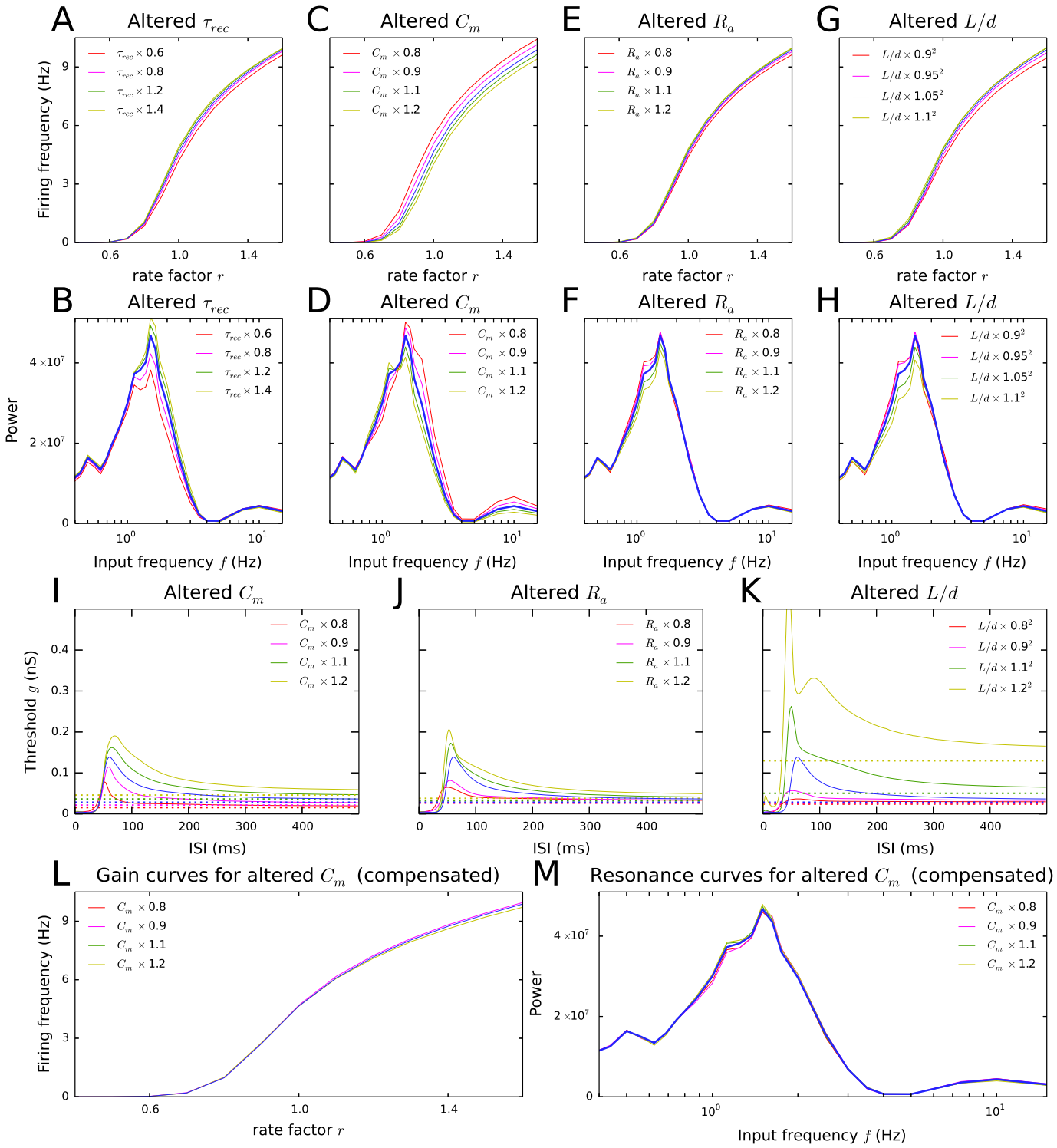
A
Altered τ_{rec}
Firing frequency (Hz)
rate factor r
B
Altered τ_{rec}
Power
Input frequency f (Hz)
C
Altered C_m
D
Altered C_m
E
Altered R_a
F
Altered R_a
G
Altered L/d
H
Altered L/d
I
Altered C_m
Threshold g (nS)
ISI (ms)
J
Altered R_a
K
Altered L/d
L
Gain curves for altered C_m (compensated)
M
Resonance curves for altered C_m (compensated)

Figure S13: **(Previous page) Effects of model parameters not related to SCZ-associated genes on L5PC network gain, response to oscillations and single-cell prepulse inhibition.** The curves represent simulation results from L5PC networks (A–H, L–M) or single L5PCs (I–K). In each simulation, the value of the model parameter describing the recovery time from short-term depression (τ_{rec}), membrane capacitance (C_m), axial resistance (R_a), or the shapes of the neurite compartments (L/d) was multiplied by a given factor. When changing the compartment shapes (L/d), the length of each compartment was multiplied by a given factor (0.9, 0.95, 1.05, or 1.1) and the diameter was divided by the same factor, which kept the membrane area fixed. Blue: control; red & magenta: decreased model-parameter values (see legends); yellow & green: increased model-parameter values (see legends). **A, C, E, G**: L5PC network gain in networks with altered recovery time from short-term depression (A), membrane capacitance (C), axial resistance (E), or neurite shapes (G). See Figure 1C. **B, D, F, H**: L5PC population response to oscillations in networks with altered recovery time from short-term depression (B), membrane capacitance (D), axial resistance (F), or neurite shapes (H). See Figure 2C. **I, J, K**: Predicted single-cell prepulse inhibition in model L5PCs with altered membrane capacitance (I), axial resistance (J), or neurite shapes (K). See Figure 5. **L, M**: L5PC population gain (L) and response to oscillations (M) in networks with altered membrane capacitance, when the effects of the altered membrane capacitance were compensated by a change in numbers of synapses ($N_{\mathrm{synE}} = 10000\alpha$ and $N_{\mathrm{synI}} = 2500\alpha$) as follows: $\tau_{rec}\times$ 0.8: $\alpha = 0.948$ (red), $\tau_{rec}\times$ 0.9: $\alpha = 0.976$ (magenta), $\tau_{rec}\times$ 1.1: $\alpha = 1.0216$ (yellow), $\tau_{rec}\times$ 1.2: $\alpha = 1.0408$ (green). These values were obtained using the bisection method in order to obtain a population firing rate for rate coefficient r=1.0 similar to that in the control L5PC network. See Figure S8 for details.

S3 Supplementary discussion

On the validity of the models

Although the Hay model (as well as the models of Almog and Korngreen, 2014 and Papoutsi et al., 2013) describes the dynamics of the intracellular Ca^{2+}, these descriptions are simple and do not account for the contributions of different Ca^{2+} buffers and transporters. Nevertheless, grand-average models of this kind can be useful in describing certain Ca^{2+}-dependent cellular phenomena. In addition to the regulation of slower processes, such as synaptic plasticity, the quantity of free Ca^{2+} ions in the intracellular medium has immediate implications on the neuron excitability due to the Ca^{2+}-dependent K^+ channels they activate. Apart from the ion channels conducting Ca^{2+}, SERCA and PMCA pumps are the key proteins coordinating the influx and efflux to/from the intracellular medium. According to the classical view, the influx of Ca^{2+} through voltage-gated Ca^{2+} channels activates the ryanodine receptors residing at the ER/SR membrane, leading to an amplification of the Ca^{2+} transients in the intracellular medium (Usachev and Thayer, 1997; Catterall, 2011). The important (although indirect) role of the SERCA protein in this calcium release was made clear in heterozygous null mutation experiments performed in myocytes, where cells with decreased SERCA expression showed much smaller Ca^{2+} transients than the control cells (see Ji et al., 2000, the data of which we used for obtaining the *ATP2A2* model variant). The role of PMCA in controlling the Ca^{2+} dynamics is more straightforward as it is the main Ca^{2+} extrusion protein — however, as it is competing with the SERCA pump for the same Ca^{2+} ions (Brini et al., 2000), the interactions between the PMCA and SERCA activity should be taken into account in future modeling work. Taken together, we consider the performed analysis on the effects of Ca^{2+}-transporter variants on neuron and neuronal network behavior a valuable proof of principle, but point out the need for application of more biochemically detailed models of neuronal Ca^{2+} dynamics alongside the biophysically detailed models of the neuron electrogenesis (Blackwell, 2013).

On L5PCs as a focus of SCZ study

In this work, we proposed the increased intrinsic L5PC activity as a SCZ-associated phenotype that could bridge genetic level observations to brain-level endophenotypes or disorder symptoms. According to our model predictions, those variants of SCZ-associated genes that increase the activity of the modeled L5PC network also decrease the threshold for second synaptic input in single-cell simulations. While this prediction could be linked to the clinical observations of deficits in prepulse inhibition of the startle reflex (see e.g. Turetsky et al., 2007), there are several questions that should first be answered:

1. Are there Ca^{2+}-dependent K^+ channels in the startle-pathway neurons? If not, the variants of Ca^{2+} channels that decreased the Ca^{2+} currents in L5PC (and thus, due to SK currents, typically increased the firing rate of the L5PC network) will not have similar effects on the neurons of the startle pathway (cf. the effects of variants in cardiac and cortical cells as studied in Mäki-Marttunen et al., 2017).

2. What is the time scale of the intracellular Ca^{2+} decay in the startle-pathway neurons? If the Ca^{2+} transients have steeper decay in startle-pathway neurons than in L5PCs, the time window of the voltage-gated ion channel-mediated prepulse inhibition will be shorter and thus different from that of the clinical prepulse inhibition.

3. How important is the voltage-gated ion channel-mediated prepulse inhibition in relation to the prepulse inhibition mediated by neurotransmission? Even if the voltage-gated ion channel-mediated mechanism we studied in L5PCs is also in place in PnC neurons, its effects could be overshadowed by the effects of the cholinergic and GABAergic inputs

to PnC neurons (see Fendt et al., 1994). This is an especially important question as genes encoding both GABAB receptor and nicotinic acetylcholine receptors are among the SCZ-associated genes (Devor et al., 2017).

To the best of our knowledge, none of the questions above have yet been answered in the literature. As for the last question, it is known that a fraction (35%–60%) of prepulse inhibition remains even if the source neurons of the cholinergic and GABAergic inputs to PnC neurons were lesioned (Fendt et al., 1994), which highlights the existence of additional mechanisms for prepulse inhibition. It should be noted that in addition to PnC neurons there are many other neuron types, including cortical neurons, that modulate the prepulse inhibition of the startle reflex (Rohleder et al., 2014). Indeed, the deficit in prepulse inhibition may represent just one example of an impaired sensory gating in SCZ patients that could be expressed in various sensory processing modalities in the affected neuron types. A detailed analysis of any of these neurons and their responses to the prepulse is, however, out of the scope of the present work.

Although increased delta-oscillation powers are one of the more robust SCZ oscillation phenotypes (Siekmeier and Stufflebeam, 2010; Moran and Hong, 2011), not all patients express them, and there exist opposite observations as well (Basar et al., 2013). A recent study suggested that the delta power is elevated in certain brain regions and weakened in others in an individual-specific manner (Hunt et al., 2017). The same can be said of the deficits in prepulse inhibition of the startle reflex: much of the variability in the strength of prepulse inhibition is affected by non-diagnostic variables, such as hormonal status, smoking, and fatigue, as well as individual variability in the brain circuits regulating PPI (Swerdlow et al., 2008). However, we believe it is important to find plausible genetically based mechanisms for the most robust SCZ phenotypes — once a general mechanism, ideally one described by computational models, is found, it will be easier to test effects of individual alterations in parallel mechanistic pathways. We propose our model of L5PCs with increased intrinsic excitability as such a genetically based mechanism. Although we have shown that it can explain clinical observations made on brain-level measurables, namely, the increased delta-band power of the EEG, the model allows one to study the effects of interacting mechanisms, which may radically alter the predicted increase in delta-band power and even reverse it, leading to the abovementioned conflicting observations (Basar et al., 2013; Hunt et al., 2017). Such interacting mechanisms could include the following:

1. Magnified downscaling of the synaptic inputs to L5PC. We showed in Figure S8 that the magnitude of increase in delta power was brought by synaptic pruning to approximately half of that in the non-pruned L5PC network. To attain this, up to 13% of the synapses (excitatory and inhibitory alike) to L5PCs were pruned. It is expected that glutamatergic and GABAergic synapses undergo different types of processes that result in them being pruned or weakened in the case of the target cell expressing too large activity (Turrigiano, 2012) (see, e.g., De Gois et al., 2005). Moreover, the alterations in synaptic strength may easily exceed the level of $\pm 13\%$ considered in this work, which could lead to a decreased delta power in comparison to a network without excitability-increasing variants and without synaptic scaling. Furthermore, the processes affecting synapse strength are known to be dependent on neuromodulatory actions (Pedrosa and Clopath, 2017), which are highly brain-area specific (cf. Picciotto et al., 2012; Bellesi et al., 2016). Therefore, we consider it likely that in certain cortical regions an excessive intrinsic excitability of L5PCs, caused by genetic variants in voltage-gated ion channel and Ca^{2+} transporter-encoding genes, may in fact lead to pruning of their synapses to the extent that they be less active than L5PCs in subjects without those specific genetic variants.

2. Magnified effects of the same or different genetic variants on interneurons. For simplicity, we considered the effects of SCZ-associated model variants only in L5PCs, although the model of Figure S9 also included inhibitory neurons. The reason for this is that the contributions of L- and T-type Ca^{2+} channels as well as HCN channels to the electrophysiological properties of cortical basket cells are largely unknown, and thus, the predicted effects of model variants in the underlying genes would be much more speculative than those made with our L5PC model. However, the variants of *SCN1A* and possibly *KCNB1* could have large effects on the excitability of interneurons, even larger than their effects on L5PCs. Given a strong coupling between interneurons and L5PCs, gain-inducing variants of these genes could decrease the firing activity of L5PCs, leading to decreased powers of the EEG signal.

3. Direct effects of neuromodulation. Risk of SCZ is associated with genetic variants in genes encoding the receptors of important neurotransmitters and neuromodulators such as dopamine, serotonin, and acetylcholine (Devor et al., 2017). As discussed above, it is possible that the effects of these neuromodulators are large in certain cortical areas under certain brain states, and that differences in the function of the underlying receptors have larger consequences on the delta-band power than the increased intrinsic excitability of L5PCs has.

4. Interacting Ca^{2+} signaling mechanisms. As mentioned before, one of our most prominent predictions is that variants that decrease the Ca^{2+} fluxes through voltage-gated Ca^{2+} channels lead to increased L5PC excitability due to the strong SK currents. However, our model does not account for the plethora of other (typically slower) intracellular signaling processes that are dependent on the levels of intracellular Ca^{2+} concentration. It is likely that some of them lead to decreased levels of L5PC activity, depending on the activity of the presynaptic neurons and the neuromodulatory state of the neuron.

Of the above three mechanisms, (1) and (2) could be tested in a straightforward manner using our model, (3) with minimal added complexity (e.g., through altered voltage-dependence of certain neuromodulation-dependent ion channels), and (4) only with an extensive modeling of intracellular cascades. However, meaningful implementation of any of these mechanisms would require an extensive analysis on the underlying *in vivo* functionalities, and therefore, we leave them for future research.

It should be noted that the effects of SCZ-associated genes that encode subunits of voltage-gated ion channels or Ca^{2+} transporters do not by any means restrict to L5PCs, and hence, many other pathways leading to (and possibly counteracting

with) the SCZ phenotypes considered here exist as well. However, there are compelling reasons for such an analysis to be made especially in L5PCs. Namely, L5PCs are likely to express the required ion channel and Ca^{2+} transporter-encoding genes (see Section S1.2.2), and they have a proven role in mediating the cortically generated delta oscillations (Carracedo et al., 2013). Moreover, due to their extensive shape, their activity may have large contributions to the EEG signal. On the other hand, the Hay model, although relatively detailed, is still lacking a deeper characterization of, e.g., different Ca^{2+}-channel subunits' contribution to the HVA Ca^{2+} current. Thus, we could not make specific model predictions on, for example, how the effects of *CACNA1C* channel variants differ from those of *CACNA1D* channel variants or variants of non-risk Ca^{2+}-channel subunit-encoding genes associated with the HVA Ca^{2+} currents. To overcome this limitation, a genetically more detailed model of ion-channel dynamics should be constructed and included in the L5PC model. Furthermore, given a better understanding on the origin and role of delta oscillations, our analysis should be accompanied by similar analyses on variant effects mediated by altered excitability of other neuron types.

References

Akemann W, Zhong Y.-M, Ichinohe N, Rockland KS, and Knöpfel T (2004). Transgenic mice expressing a fluorescent In Vivo label in a distinct subpopulation of neocortical layer 5 pyramidal cells. J Comp Neurol, 480 (1): 72–88.

Almog M and Korngreen A (2014). A quantitative description of dendritic conductances and its application to dendritic excitation in layer 5 pyramidal neurons. J Neurosci, 34 (1): 182–196.

Almog M, Korngreen A, et al. (2009). Characterization of voltage-gated Ca (2+) conductances in layer 5 neocortical pyramidal neurons from rats. PLoS ONE, 4 (4): e4841–e4841.

Atallah BV, Bruns W, Carandini M, and Scanziani M (2012). Parvalbumin-expressing interneurons linearly transform cortical responses to visual stimuli. Neuron, 73 (1): 159–170.

Azizan EA, Poulsen H, Tuluc P, Zhou J, Clausen MV, Lieb A, Maniero C, Garg S, Bochukova EG, Zhao W, et al. (2013). Somatic mutations in ATP1A1 and CACNA1D underlie a common subtype of adrenal hypertension. Nat Genet, 45 (9): 1055–1060.

Baba-Aissa F, Raeymaekers L, Wuytack F, Dode L, and Casteels R (1998). Distribution and isoform diversity of the organellar Ca2+ pumps in the brain. Mol Chem Neuropathol, 33 (3): 199–208.

Ballesteros-Merino C, Watanabe M, Shigemoto R, Fukazawa Y, Adelman JP, and Luján R (2014). Differential subcellular localization of SK3-containing channels in the hippocampus. European J Neurosci, 39 (6): 883–892.

Basar E, Basar-Eroglu C, Guntekin B, and Yener GG (2013). Brain's alpha, beta, gamma, delta, and theta oscillations in neuropsychiatric diseases: proposal for biomarker strategies. Suppl Clin Neurophysiol, 62 (1).

Battefeld A, Tran BT, Gavrilis J, Cooper EC, and Kole MH (2014). Heteromeric Kv7. 2/7.3 channels differentially regulate action potential initiation and conduction in neocortical myelinated axons. J Neurosci, 34 (10): 3719–3732.

Bellesi M, Tononi G, Cirelli C, and Serra PA (2016). Region-specific dissociation between cortical noradrenaline levels and the sleep/wake cycle. Sleep, 39 (1): 143–154.

Blackwell K (2013). Approaches and tools for modeling signaling pathways and calcium dynamics in neurons. J Neurosci Methods, 220 (2): 131–140.

Bock G, Gebhart M, Scharinger A, Jangsangthong W, Busquet P, Poggiani C, Sartori S, Mangoni ME, Sinnegger-Brauns MJ, Herzig S, et al. (2011). Functional properties of a newly identified C-terminal splice variant of Cav1. 3 L-type Ca2+ channels. J Biol Chem, 286 (49): 42736–42748.

Bocksteins E, Ottschytsch N, Timmermans J.-P, Labro A, and Snyders D (2011). Functional interactions between residues in the S1, S4, and S5 domains of Kv2.1. Eur Biophys J, 40 (6): 783–793.

Brini M, Bano D, Manni S, Rizzuto R, and Carafoli E (2000). Effects of PMCA and SERCA pump overexpression on the kinetics of cell Ca 2+ signalling. The EMBO J, 19 (18): 4926–4935.

Buetfering C, Allen K, and Monyer H (2014). Parvalbumin interneurons provide grid cell-driven recurrent inhibition in the medial entorhinal cortex. Nat Neurosci, 17 (5): 710–718.

Carracedo LM, Kjeldsen H, Cunnington L, Jenkins A, Schofield I, Cunningham MO, Davies CH, Traub RD, and Whittington MA (2013). A neocortical delta rhythm facilitates reciprocal interlaminar interactions via nested theta rhythms. J Neurosci, 33 (26): 10750–10761.

Catterall WA (2011). Voltage-gated calcium channels. Cold Spring Harbor Perspect Biol, 3 (8): a003947.

Catterall WA, Perez-Reyes E, Snutch TP, and Striessnig J (2005). International Union of Pharmacology. XLVIII. Nomenclature and structure-function relationships of voltage-gated calcium channels. Pharmacol Rev, 57 (4): 411–425.

Cestèle S, Labate A, Rusconi R, Tarantino P, Mumoli L, Franceschetti S, Annesi G, Mantegazza M, and Gambardella A (2013). Divergent effects of the T1174S SCN1A mutation associated with seizures and hemiplegic migraine. Epilepsia, 54 (5): 927–935.

Cestèle S, Scalmani P, Rusconi R, Terragni B, Franceschetti S, and Mantegazza M (2008). Self-limited hyperexcitability: Functional effect of a familial hemiplegic migraine mutation of the Nav1.1 (SCN1A) Na+ channel. J Neurosci, 28 (29): 7273–7283.

Chen I.-W, Helmchen F, and Lütcke H (2015). Specific early and late oddball-evoked responses in excitatory and inhibitory neurons of mouse auditory cortex. J Neurosci, 35 (36): 12560–12573.

Chen J.-R, Wang B.-N, Tseng G.-F, Wang Y.-J, Huang Y.-S, and Wang T.-J (2014). Morphological changes of cortical pyramidal neurons in hepatic encephalopathy. BMC neuroscience, 15 (1): 15.

Christophe E, Doerflinger N, Lavery DJ, Molnár Z, Charpak S, and Audinat E (2005). Two populations of layer V pyramidal cells of the mouse neocortex: development and sensitivity to anesthetics. J Neurophysiol, 94 (5): 3357–3367.

Cordeiro JM, Marieb M, Pfeiffer R, Calloe K, Burashnikov E, and Antzelevitch C (2009). Accelerated inactivation of the L-type calcium current due to a mutation in CACNB2b underlies Brugada syndrome. J Mol Cell Cardiol, 46 (5): 695–703.

De Gois S, Schäfer MK.-H, Defamie N, Chen C, Ricci A, Weihe E, Varoqui H, and Erickson JD (2005). Homeostatic scaling of vesicular glutamate and GABA transporter expression in rat neocortical circuits. J Neurosci, 25 (31): 7121–7133.

Depil K, Beyl S, Stary-Weinzinger A, Hohaus A, Timin E, and Hering S (2011). Timothy mutation disrupts the link between activation and inactivation in Cav1. 2 protein. J Biol Chem, 286 (36): 31557–31564.

Devor A, Andreassen O, Wang Y, Mäki-Marttunen T, Smeland O, Fan C, Schork A, Holland D, Thompson W, Witoelar A, et al. (2017). Genetic evidence for role of integration of fast and slow neurotransmission in schizophrenia. Mol Psychiatry, 22 (6): 792.

Empson RM, Akemann W, and Knöpfel T (2010). The role of the calcium transporter protein plasma membrane calcium ATPase PMCA2 in cerebellar Purkinje neuron function. Funct Neurol, 25 (3): 153.

Fakira AK, Gaspers LD, Thomas AP, Li H, Jain MR, and Elkabes S (2012). Purkinje cell dysfunction and delayed death in plasma membrane calcium ATPase 2-heterozygous mice. Mol Cell Neurosci, 51 (1): 22–31.

Fendt M, Li L, and Yeomans JS (1994). Brain stem circuits mediating prepulse inhibition of the startle reflex. Psychopharmacology, 156 (2–3): 216–224.

Ficarella R, Di Leva F, Bortolozzi M, Ortolano S, Donaudy F, Petrillo M, Melchionda S, Lelli A, Domi T, Fedrizzi L, et al. (2007). A functional study of plasma-membrane calcium-pump isoform 2 mutants causing digenic deafness. Proc Natl Acad Sci USA, 104 (5): 1516–1521.

Fuhrmann G, Segev I, Markram H, and Tsodyks M (2002). Coding of temporal information by activity-dependent synapses. J Neurophysiol, 87 (1): 140–148.

Galarreta M and Hestrin S (2002). Electrical and chemical synapses among parvalbumin fast-spiking GABAergic interneurons in adult mouse neocortex. Proc Natl Acad Sci USA, 99 (19): 12438–12443.

Geisler S, Schöpf CL, and Obermair GJ (2015). Emerging evidence for specific neuronal functions of auxiliary calcium channel $\alpha 2\delta$ subunits. Gen Physiol Biophys, 34 (2): 105.

Giacomello M, De Mario A, Lopreiato R, Primerano S, Campeol M, Brini M, and Carafoli E (2011). Mutations in PMCA2 and hereditary deafness: a molecular analysis of the pump defect. Cell Calcium, 50 (6): 569–576.

Gomora JC, Murbartian J, Arias JM, Lee J.-H, and Perez-Reyes E (2002). Cloning and expression of the human T-type channel Ca v 3.3: insights into prepulse facilitation. Biophys J, 83 (1): 229–241.

Guan D, Tkatch T, Surmeier D, Armstrong W, and Foehring R (2007). Kv2 subunits underlie slowly inactivating potassium current in rat neocortical pyramidal neurons. J Physiol (Lond), 581 (3): 941–960.

Hay E, Hill S, Schürmann F, Markram H, and Segev I (2011). Models of neocortical layer 5b pyramidal cells capturing a wide range of dendritic and perisomatic active properties. PLoS Comput Biol, 7: e1002107.

Hay E and Segev I (2015). Dendritic Excitability and Gain Control in Recurrent Cortical Microcircuits. Cereb Cortex, 25 (10): 3561–3571.

Hohaus A, Beyl S, Kudrnac M, Berjukow S, Timin EN, Marksteiner R, Maw MA, and Hering S (2005). Structural determinants of L-type channel activation in segment IIS6 revealed by a retinal disorder. J Biol Chem, 280 (46): 38471–38477.

Hu D, Barajas-Martinez H, Nesterenko VV, Pfeiffer R, Guerchicoff A, Cordeiro JM, Curtis AB, Pollevick GD, Wu Y, Burashnikov E, et al. (2010). Dual variation in SCN5A and CACNB2b underlies the development of cardiac conduction disease without Brugada syndrome. Pacing Clin Electrophysiol, 33 (3): 274–285.

Hunt MJ, Kopell NJ, Traub RD, and Whittington MA (2017). Aberrant Network Activity in Schizophrenia. Trends Neurosci.

Ishii TM, Nakashima N, and Ohmori H (2007). Tryptophan-scanning mutagenesis in the S1 domain of mammalian HCN channel reveals residues critical for voltage-gated activation. J Physiol (Lond), 579 (2): 291–301.

Jahr CE and Stevens CF (1990). Voltage dependence of NMDA-activated macroscopic conductances predicted by single-channel kinetics. J Neurosci, 10 (9): 3178–3182.

Ji Y, Lalli MJ, Babu GJ, Xu Y, Kirkpatrick DL, Liu LH, Chiamvimonvat N, Walsh RA, Shull GE, and Periasamy M (2000). Disruption of a single copy of the SERCA2 gene results in altered Ca2+ homeostasis and cardiomyocyte function. J Biol Chem, 275 (48): 38073–38080.

Kudrnac M, Beyl S, Hohaus A, Stary A, Peterbauer T, Timin E, and Hering S (2009). Coupled and independent contributions of residues in IS6 and IIS6 to activation gating of CaV1.2. J Biol Chem, 284 (18): 12276–12284.

Lee SH, DeCandia TR, Ripke S, Yang J, Sullivan PF, Goddard ME, Keller MC, Visscher PM, Wray NR, Schizophrenia Psychiatric Genome-Wide Association Study Consortium, et al. (2012). Estimating the proportion of variation in susceptibility to schizophrenia captured by common SNPs. Nat Genet, 44 (3): 247–250.

Lesso H and Li RA (2003). Helical secondary structure of the external S3-S4 linker of pacemaker (HCN) channels revealed by site-dependent perturbations of activation phenotype. J Biol Chem, 278 (25): 22290–22297.

Lieb A, Scharinger A, Sartori S, Sinnegger-Brauns MJ, and Striessnig J (2012). Structural determinants of CaV1. 3 L-type calcium channel gating. Channels, 6 (3): 197–205.

Link S, Meissner M, Held B, Beck A, Weissgerber P, Freichel M, and Flockerzi V (2009). Diversity and developmental expression of L-type calcium channel $\beta 2$ proteins and their influence on calcium current in murine heart. J Biol Chem, 284 (44): 30129–30137.

Ma JY, Catterall WA, and Scheuer T (1997). Persistent sodium currents through brain sodium channels induced by G protein $\beta\gamma$ subunits. Neuron, 19 (2): 443–452.

Mäki-Marttunen T, Halnes G, Devor A, Metzner C, Dale AM, Andreassen OA, and Einevoll GT (2018). A stepwise neuron model fitting procedure designed for recordings with high spatial resolution: Application to layer 5 pyramidal cells. J Neurosci Methods, 273: 264–283.

Mäki-Marttunen T, Halnes G, Devor A, Witoelar A, Bettella F, Djurovic S, Wang Y, Einevoll GT, Andreassen OA, and Dale AM (2016). Functional effects of schizophrenia-linked genetic variants on intrinsic single-neuron excitability: A modeling study. Biol Psychiatry Cogn Neurosci Neuroim, 1 (1): 49–59.

Mäki-Marttunen T, Lines GT, Edwards AG, Tveito A, Dale AM, Einevoll GT, and Andreassen OA (2017). Pleiotropic effects of schizophrenia-associated genetic variants in neuron firing and cardiac pacemaking revealed by computational modeling. Transl Psychiatry, 7: 5.

Mantegazza M, Gambardella A, Rusconi R, Schiavon E, Annesi F, Cassulini RR, Labate A, Carrideo S, Chifari R, Canevini MP, et al. (2005). Identification of an Nav1.1 sodium channel (SCN1A) loss-of-function mutation associated with familial simple febrile seizures. Proc Natl Acad Sci USA of the United States of America, 102 (50): 18177–18182.

Markram H, Muller E, Ramaswamy S, Reimann MW, Abdellah M, Sanchez CA, Ailamaki A, Alonso-Nanclares L, Antille N, Arsever S, et al. (2015). Reconstruction and simulation of neocortical microcircuitry. Cell, 163 (2): 456–492.

Massa E, Kelly KM, Yule DI, MacDonald RL, and Uhler MD (1995). Comparison of fura-2 imaging and electrophysiological analysis of murine calcium channel alpha 1 subunits coexpressed with novel beta 2 subunit isoforms. Mol Pharmacol, 47 (4): 707–716.

Meyer HS, Wimmer VC, Oberlaender M, De Kock CP, Sakmann B, and Helmstaedter M (2010). Number and laminar distribution of neurons in a thalamocortical projection column of rat vibrissal cortex. Cereb Cortex, 20 (10): 2277–2286.

Moore AK and Wehr M (2013). Parvalbumin-expressing inhibitory interneurons in auditory cortex are well-tuned for frequency. J Neurosci, 33 (34): 13713–13723.

Moran LV and Hong LE (2011). High vs low frequency neural oscillations in schizophrenia. Schizophr Bull, 37 (4): 659–663.

Murbartián J, Arias JM, and Perez-Reyes E (2004). Functional impact of alternative splicing of human T-type Cav3.3 calcium channels. J Neurophysiol, 92 (6): 3399–3407.

Næss S, Chintaluri HC, Ness TV, Dale AM, Einevoll GT, and Wójcik DK (2017). Corrected four-sphere head model for EEG signals. Front Hum Neurosci, 11: 490.

Papoutsi A, Sidiropoulou K, Cutsuridis V, and Poirazi P (2013). Induction and modulation of persistent activity in a layer V PFC microcircuit model. Front Neural Circuits, 7: 161.

Pedrosa V and Clopath C (2017). The role of neuromodulators in cortical plasticity. a computational perspective. Front Synaptic Neurosci, 8: 38.

Pérez-Alvarez A, Hernández-Vivanco A, Caba-González JC, and Albillos A (2011). Different roles attributed to Cav1 channel subtypes in spontaneous action potential firing and fine tuning of exocytosis in mouse chromaffin cells. J Neurochem, 116 (1): 105–121.

Picciotto MR, Higley MJ, and Mineur YS (2012). Acetylcholine as a neuromodulator: cholinergic signaling shapes nervous system function and behavior. Neuron, 76 (1): 116–129.

Pinggera A, Lieb A, Benedetti B, Lampert M, Monteleone S, Liedl KR, Tuluc P, and Striessnig J (2015). CACNA1D De Novo Mutations in Autism Spectrum Disorders Activate Cav1. 3 L-Type Calcium Channels. Biol Psychiatry, 77 (9): 816–822.

Pospischil M, Toledo-Rodriguez M, Monier C, Piwkowska Z, Bal T, Frégnac Y, Markram H, and Destexhe A (2008). Minimal Hodgkin–Huxley type models for different classes of cortical and thalamic neurons. Biol Cybern, 99 (4): 427–441.

Ripke S et al. (2014). Biological insights from 108 schizophrenia-associated genetic loci. Nature, 511 (7510): 421–427.

Rohleder C, Jung F, Mertgens H, Wiedermann D, Sué M, Neumaier B, Graf R, Leweke FM, and Endepols H (2014). Neural correlates of sensorimotor gating: a metabolic positron emission tomography study in awake rats. Front Behav Neurosci, 8: 178.

Rosati B and McKinnon D (2004). Regulation of ion channel expression. Circ Res, 94 (7): 874–883.

Siekmeier PJ and Stufflebeam SM (2010). Patterns of spontaneous magnetoencephalographic activity in schizophrenic patients. J Clin Neurophysiol, 27 (3): 179.

Somogyi P, Tamas G, Lujan R, and Buhl EH (1998). Salient features of synaptic organisation in the Cereb Cortex1. Brain Res Rev, 26 (2-3): 113–135.

Srinivasan R, Nunez PL, and Silberstein RB (1998). Spatial filtering and neocortical dynamics: estimates of EEG coherence. IEEE Transactions on Biomed Eng, 45 (7): 814–826.

Stahl WL, Eakin TJ, Owens JW, Breininger JF, Filuk PE, and Anderson WR (1992). Plasma membrane Ca 2+-ATPase isoforms: distribution of mRNAs in rat brain by in situ hybridization. Mol Brain Res, 16 (3): 223–231.

Stahl WL, Keeton TP, and Eakin TJ (1994). The plasma membrane Ca 2+-ATPase mRNA isoform PMCA 4 is expressed at high levels in neurons of rat piriform cortex and neocortex. Neurosci Lett, 178 (2): 267–270.

Stary A, Kudrnac M, Beyl S, Hohaus A, Timin E, Wolschann P, Guy HR, and Hering S (2008). Molecular dynamics and mutational analysis of a channelopathy mutation in the IIS6 helix of Cav1. 2. Channels, 2 (3): 216–223.

Swerdlow NR, Weber M, Qu Y, Light GA, and Braff DL (2008). Realistic expectations of prepulse inhibition in translational models for Schizophr Res. Psychopharmacology, 199 (3): 331–388.

Tan BZ, Jiang F, Tan MY, Yu D, Huang H, Shen Y, and Soong TW (2011). Functional characterization of alternative splicing in the C terminus of L-type CaV1. 3 channels. J Biol Chem, 286 (49): 42725–42735.

Tang ZZ, Liang MC, Lu S, Yu D, Yu CY, Yue DT, and Soong TW (2004). Transcript scanning reveals novel and extensive splice variations in human L-type voltage-gated calcium channel, Cav1. 2 α1 subunit. J Biol Chem, 279 (43): 44335–44343.

Tian C, Wang K, Ke W, Guo H, and Shu Y (2014). Molecular identity of axonal sodium channels in human cortical pyramidal cells. Front Cell Neurosci, 8: 297.

Tran-Gia P (1983). "Simulation of instationary processes for performance evaluations of switching systems". In: *First European Simulation Congress ESC 83*. Springer, pp. 362–367.

Turetsky BI, Calkins ME, Light GA, Olincy A, Radant AD, and Swerdlow NR (2007). Neurophysiological endophenotypes of schizophrenia: the viability of selected candidate measures. Schizophr Bull, 33 (1): 69–94.

Turrigiano G (2012). Homeostatic synaptic plasticity: local and global mechanisms for stabilizing neuronal function. Cold Spring Harbor Perspect Biol, 4 (1): a005736.

Usachev YM and Thayer SA (1997). All-or-none Ca2+ release from intracellular stores triggered by Ca2+ influx through voltage-gated Ca2+ channels in rat sensory neurons. J Neurosci, 17 (19): 7404–7414.

Vanmolkot KR, Babini E, Vries B de, Stam AH, Freilinger T, Terwindt GM, Norris L, Haan J, Frants RR, Ramadan NM, et al. (2007). The novel p.L1649Q mutation in the SCN1A epilepsy gene is associated with familial hemiplegic migraine: genetic and functional studies. Hum Mutat, 28 (5): 522–522.

Volkers L, Kahlig KM, Verbeek NE, Das JH, Kempen MJ van, Stroink H, Augustijn P, Nieuwenhuizen O van, Lindhout D, George AL, et al. (2011). Nav1. 1 dysfunction in genetic epilepsy with febrile seizures-plus or Dravet syndrome. European J Neurosci, 34 (8): 1268–1275.

Wemhöner K, Kanyshkova T, Silbernagel N, Fernandez-Orth J, Bittner S, Kiper AK, Rinné S, Netter MF, Meuth SG, Budde T, et al. (2015). An N-terminal deletion variant of HCN1 in the epileptic WAG/Rij strain modulates HCN current densities. Front Mol Neurosci, 8: 83.

Whitaker WR, Clare JJ, Powell AJ, Chen YH, Faull RL, and Emson PC (2000). Distribution of voltage-gated sodium channel α-subunit and β-subunit mRNAs in human hippocampal formation, cortex, and cerebellum. J Comp Neurol, 422 (1): 123–139.

Zhang Q, Timofeyev V, Qiu H, Lu L, Li N, Singapuri A, Torado CL, Shin HS, and Chiamvimonvat N (2011). Expression and roles of Cav1.3 (α1D) L-type Ca2+ channel in atrioventricular node automaticity. J Mol Cell Cardiol, 50 (1): 194–202.

Zhou F.-W and Roper SN (2010). Altered firing rates and patterns in interneurons in experimental cortical dysplasia. Cereb Cortex, 21 (7): 1645–1658.